TECHNISCHE
UNIVERSITÄT
WIEN
Vienna | Austria

## Master Thesis

# Solutal convection in two-dimensional porous media

carried out for the purpose of obtaining the degree of Master of Science (MSc or Dipl.-Ing. or DI), submitted at TU Wien, Faculty of Mechanical and Industrial Engineering, by

**LEA ROSA ENZENBERGER**

Mat.Nr.: 01568330

under the supervision of

Prof. Sergio Pirozzoli

Dr. Francesco Zonta

Dr. Marco De Paoli

Prof. Alfredo Soldati

Institute of Fluid Mechanics and Heat Transfer, E322

Vienna, June 2024

# Affidavit

I declare in lieu of oath, that I wrote this thesis and carried out the associated research myself, using only the literature cited in this volume. If text passages from sources are used literally, they are marked as such. I confirm that this work is original and has not been submitted for examination elsewhere, nor is it currently under consideration for a thesis elsewhere. I acknowledge that the submitted work will be checked electronically-technically using suitable and state-of-the-art means (plagiarism detection software). On the one hand, this ensures that the submitted work was prepared according to the high-quality standards within the applicable rules to ensure good scientific practice "Code of Conduct" at the TU Wien. On the other hand, a comparison with other student theses avoids violations of my personal copyright.

Vienna, June 30, 2024

. . . . . . . . . . . . . . . . . . . . . .

Signature

# Acknowledgments

First, I want to thank Prof. Alfredo Soldati, Dr. Francesco Zonta and Prof. Sergio Pirozzoli for making it possible to do the biggest part of the work that went into this thesis in Rome. It was an unforgettable and educational experience that I would not want to miss. I also want to point out that the time Dr. Zonta, Prof. Pirozzoli, and not to forget Dr. Marco de Paoli, carved out each and every week to give support and answer questions was invaluable to the progress of this work and I want to say a genuine thank you to the three of them for that. Furthermore, I want to express my gratitude towards Eliza Coliban who has supported me in plenty of different ways, the subject-specific one being only a part. Lastly, I want to highlight how fortunate we are to have the European Union, which makes exchanges like this possible and fosters both professional and personal connections.

# Abstract

Carbon dioxide is one of the most effective greenhouse gases, promoting global warming with its increasing atmospheric concentration. To reduce the amount of $CO_2$ present in the atmosphere, and emitted primarily by fossil fuel combustion, there is the possibility of Carbon Dioxide Capture and Storage (CCS). This entails the injection of supercritical $CO_2$ into deep geological formations. Being liquid in its supercritical state, liquid $CO_2$ dissolves and mixes with the brine (i.e. water with a high concentration of salt) already present in these reservoirs. The dissolution process produces a solute that is heavier than brine, and that falls down by gravity, making it attractive for the permanent $CO_2$ storage. However, the efficiency of the process, and its correct prediction via suitable numerical simulations is still to be fully understood.

For this reason, in the present thesis, we simulate the process of solute convection in a two-dimensional domain, assuming solute injection from the top boundary, and impermeable conditions at the bottom boundary (one-sided configuration). Simulations are run for different reservoir sizes and grid resolutions, in order to assess the quality of the results by looking at the time-dependent flow development – including flow structure sizes, and measures of mixing. Current results compare well with literature results, and pave the way for future three-dimensional investigations in the field.

# Zusammenfassung

Kohlendioxid zählt zu den klimawirksamsten Treibhausgasen, dessen steigender Gehalt in der Atmosphäre die Erderwärmung immer weiter vorantreibt. Um die Umstellung auf ausschließlich erneuerbare Energien in der Stromerzeugung zu erleichtern indem weiterhin fossile Brennstoffe verwendet werden oder den Abgasausstoß stark emmittierender Industrieprozesse zu mindern gibt es die Möglichkeit der sogenannten $CO_2$-Abscheidung und Speicherung oder CCS (englisch für Carbon Dioxide Capture and Storage). Dabei wird das $CO_2$ in superkritischen Zustand gebracht und in tief unter der Erde liegende geologische Formationen eingebracht. Im superkritischen Zustand flüssig, vermischt es sich mit in den Formationen schon vorhandener Sole (Wasser mit einer hohen Konzentration an Salz). Der Auflösungsprozess produziert eine Lösung, die eine höhere Dichte aufweist, als die beiden Flüssigkeiten alleine und somit von der Schwerkraft nach unten gezogen wird, was die Sicherheit der Lagerung stark erhöht. Um eine bessere Abschätzung der Mechanismen und Zeiträume der Strömungsentwicklung zu bekommen können computergestützte Berechnungen durchgeführt werden, die die Vorkommnisse simulieren.

In dieser Arbeit wird deshalb der Prozess der lösenden Konvektion in einer zweidimensionalen Domäne simuliert. Die Einbringung erfolgt von der oberen Grenze, die untere Grenze wird durch eine Undurchlässigkeitsbedingung definiert (einseitige Konfiguration). Die Vorgänge werden für unterschiedliche Reservoirgrößen und Gitterauflösungen simuliert, um die zeitlich abhängige Entwicklung der Strömung, die Größen der entstehenden Strömungsstrukturen und Mischungsmaße näher zu betrachten. Die gute Übereinstimmung der erhaltenen Ergebnisse mit bereits veröffentlichten Resultaten ermöglicht die Erweiterung zu dreidimensionalen Untersuchungen des Problems in der Zukunft.

# Contents

**1 Introduction** **1**

**2 Methodology** **11**

2.1 Model . . . . . . . . . . . . . . . . . . . . . . . . . . . . . . . . . . 11

2.1.1 Governing Equations . . . . . . . . . . . . . . . . . . . . . . . 12

2.2 Numerical Methods . . . . . . . . . . . . . . . . . . . . . . . . . . . . 14

2.3 Assessment of grid resolution and domain size . . . . . . . . . . . . . . 15

2.3.1 Grid sensitivity study . . . . . . . . . . . . . . . . . . . . . . . 15

2.3.2 Boundary effects . . . . . . . . . . . . . . . . . . . . . . . . . 18

2.4 Computational Details . . . . . . . . . . . . . . . . . . . . . . . . . . 20

**3 Results** **23**

3.1 Flow Field Visualization and Flow Structures . . . . . . . . . . . . . . 23

3.1.1 Flow Field . . . . . . . . . . . . . . . . . . . . . . . . . . . . . 23

3.1.2 Size of flow structures . . . . . . . . . . . . . . . . . . . . . . 27

3.2 Identification of Flow Regimes . . . . . . . . . . . . . . . . . . . . . . 29

3.2.1 Diffusion-dominated regime . . . . . . . . . . . . . . . . . . . 30

3.2.2 Convection-dominated regime . . . . . . . . . . . . . . . . . . 31

3.2.3 Shutdown Regime . . . . . . . . . . . . . . . . . . . . . . . . . 37

3.3 Measures of Mixing . . . . . . . . . . . . . . . . . . . . . . . . . . . . 40

3.3.1 Mean scalar dissipation rate $\langle\chi\rangle$ . . . . . . . . . . . . . . . . . 40

3.3.2 Mixing Rate $\frac{\partial\langle C^2\rangle}{\partial t}$ . . . . . . . . . . . . . . . . . . . . . . 42

3.3.3 Mean wavenumber . . . . . . . . . . . . . . . . . . . . . . . . 42

3.3.4 Intensity of Segregation . . . . . . . . . . . . . . . . . . . . . 43

3.3.5 Concentration Variance . . . . . . . . . . . . . . . . . . . . . . 44

3.4 Influence of Rayleigh Darcy number . . . . . . . . . . . . . . . . . . . 44

3.4.1 Dissolution Flux . . . . . . . . . . . . . . . . . . . . . . . . . . 44

3.4.2 Characteristic length scale of flow structures . . . . . . . . . . . 48

4 Conclusion 50

Nomenclature 53

List of Figures 58

List of Tables 59

Bibliography 60

# 1

# Introduction

Until now, the greenhouse effect has kept our earth a habitable environment. The so-called greenhouse gases let the short-wave sunbeams through the atmosphere onto earths surface but keep the long-wave thermal radiation inside, ensuring appropriate temperatures for plants, animals and humans. One of those greenhouse gases is Carbon dioxide ($CO_2$) which, being present in increasingly high concentrations in the atmosphere, has a remarkable effect on climate changes, since it makes the earth warmer. As of today, the atmospheric concentration of $CO_2$ (measured by the Oceanic and Atmospheric Research, OAR [1]) is 0.0422%. That is an increase of about 45% since the start of the industrial revolution, supporting the fact that all these emissions are human made [6]. Additionally, the amount of anthropogenic emissions per year rises every year as well, making the amount of $CO_2$ in the atmosphere higher and higher. The uncertainties and generally bad predictions linked to the effects of global warming are a reason to work on the reduction of carbon emissions. The ideas and projects trying for mitigation are different but have to be used together, since no method will solve the problem on its own. To reduce the amount of carbon dioxide that is released into the atmosphere, the straightforward way might be to reduce the amount of used energy and resources and migrate to renewable energies for power production. A different further mitigation method, where no big changes in current habits would be needed, is the sequestration of the produced carbon dioxide [33]. This is usually referred to as carbon dioxide capture and storage (CCS). It is the capture of $CO_2$ from power plants and industrial processes, its transport and finally its storage in suitable deposits. In this way, already existing and established infrastructure could still be used after some adjustments, and available fossil fuels could be further exploited, limiting the cost of climate change mitigation methods [34]. However, it should not be forgotten that approximately 800 large coal-fired power plants would have to be refurbished with $CO_2$ capturing equipment and store their produced $CO_2$ to make a difference of only one climate stabilization wedge [6] meaning 25 gigatons of avoided carbon dioxide emissions over a fifty-year period [31]. This method also only works for fixed $CO_2$-emitters, while for moving ones like cars or planes, the capture is not possible. Reason is the three times higher weight of $CO_2$ in comparison with fuel, making it unfeasible to capture during movement [33]. There also remains the issue of cost. Prices of energy production with downstream CCS are increased by about 70 to 100 %, the cost of capture and compression constituting the biggest part [34]. This is due to the fact that with current technology about 30 % of the power plant's produced energy is needed for the CCS operations. Additionally, in a power plant with capturing facilities, the need of cooling water is doubled compared to a regular power plant [6].

The avoidance of further emissions should however make all these difficulties seem small, since the price to pay for a further progression of global warming is unforeseeable. To better understand the problem, the first part of this work is dedicated to a deeper explanation of CCS and what possibilities of storage there are available.

The capture is easiest at places of considerable $CO_2$ release. Examples are the power generation through combustion of fossil fuels or through biomass, natural gas processing, the preparation of fossil fuels and the production of iron, steel, cement or hydrogen where it gets separated from other elements of the exhaust gases [33, 34]. Suitable locations for storage are often not directly at the $CO_2$-emitting industries, which make transportation necessary. Especially the relocation by pipeline is favorable since knowledge and infrastructure regarding the transport of gases are already existing. Another way for long distance transport is using ships [34]. Storage then means pressurizing the $CO_2$ to achieve a supercritical state and removing it from the atmosphere. Objective is the opportunity of storing a considerable amount of $CO_2$ to make it be worthwhile for the longest possible time. Especially when looking at one certain emitter, the chosen formation has to have sufficient capacity, e.g. for the $CO_2$ produced over the lifetime of the emitter [6]. In the meantime, the process has to be safe throughout the whole sequestration timespan. Not only during injection, no $CO_2$ can escape, but also it has to remain securely in the storage site for the planned period of time. Reasons for the need of this enhanced security lie in the severe impacts of carbon dioxide leakage.

Contamination of the atmosphere, neighboring rock formations, soil and/or groundwater reservoirs with $CO_2$ can lead to denatured drinking-water as well as negative effects on flora and fauna around the exit point of the escaped $CO_2$ [6, 7].

There are different possibilities for the storage of $CO_2$ [7, 34]:

- geological structures underground
    - depleted oil or gas reservoirs
    - deep coal seams
    - deep saline aquifers
- ocean
- mineral carbonates

For storage in formations underground the same technologies already used in the oil and gas industry can get deployed. Usable geological structures are sedimentary basins, both onshore and offshore. Preconditions for a suitable basin are permeable rock formations, empty or saturated with saline water - in which case they are called saline formations -, structural simplicity and the presence of a non-permeable low porosity layer on top acting as a seal [34]. The permeable part often consists of sandstones and carbonates, while non-permeable parts entail shales, anhydrides and salt beds. It is important that there are no faults or fractures in this so-called impermeable caprock or else the $CO_2$ easily escapes [6, 34]. The reservoirs should furthermore be located at adequate depths, making the pressure inside high enough so that the injected $CO_2$ stays supercritical or liquid. This means a positioning of the reservoir between 600 and 3000 m under the earth or the sea floor [2, 17].

In depleted oil and gas reservoirs these prerequisites are already known to be present, since for ages oil or gas was safely enclosed there. Additionally, the structures are well known and infrastructure is already there, ready to use [34]. Another reason why the storage in these reservoirs might be favorable is the enhanced oil or else gas recovery (EOR or EGR). During this procedure a gas is injected into the almost empty reservoirs, pushing the remaining fossil fuel towards the extraction wells thereby facilitating economic gains [33]. This would in theory be a favorable combination of processes but bears the difficulty of timing. The sites have to be nearly depleted at injection start and so there arises the need of storage of the $CO_2$ until that time has come [34]. Furthermore there is the risk of leakage through the many wells that were previously used to pump up the oil or gas [6].

Coal seams on first glance also seem like a favorable storage for $CO_2$ since it exhibits a strong sorption towards coal and therefore ensures secure trapping. Unfortunately coal swells when in contact with $CO_2$, reducing permeability and so capacity gravely. On top of this, coal beds that lie deep enough underground for the use of CCS are already low in permeability from the start, making them essentially unusable [6].

Saline aquifers on the other hand are readily available at many places in the world and offer a satisfactory capacity for large-scale injections [6]. A potential storage capacity of at least 2000 Gt carbon dioxide is expected in geological formations. Due to the difficulty to assess the actual dimensions of saline formations, this estimate is rather on the lower end of the scale [34].

The second and third option of storage, mineral carbonation and deposition of $CO_2$ in the ocean are not well researched yet, but seem to be suboptimal when exploring them in detail. In great depths of the ocean, the liquid $CO_2$ forms pools and would therefore be sealed off from the atmosphere. This deposition in the sea however entails a change in the pH value of the surrounding waters, which in turn has a bad effect on the mortality of ocean creatures. With an elevated amount of stored $CO_2$ the chemistry in the entire ocean would get measurably changed [34]. Additionally, storage times are rather short, making this method unfeasible [33].

Meanwhile, the mineralization of $CO_2$ is the most permanent and thus safest option, since the carbonic acid is getting neutralized by forming carbonates and bicarbonates [33]. Nevertheless, to achieve mineral carbonation the right minerals have to be quarried in surface mines, which entails the need of clearing of land with negative effects on water and vegetation and a decrease in local air quality.

The best suited storage sites therefore seem to be underground geological formations. There, stratification is stable for the longest time and the biggest amount of carbon dioxide can be stored out of the three options. Especially the saline formations are exhibiting a big potential and are estimated to have capacity to store emissions for at least one century [6, 7, 33, 34, 38]. They can be found in many places on earth, easing the further challenge of transportation of the isolated $CO_2$. Even though they are essentially containing water in the form of saline brine, it is non-usable for both agriculture and human consumption [34]. All these above-mentioned reasons point to the utilization of the saline aquifers. Having the prerequisites for safe capture, to ensure permanent safety, long-term storage behavior, more precisely the possible migration of liquid $CO_2$, needs to be understood better and more thoroughly. Due to the high cost of CCS it is also important to get insight into the minimum timescale of storage to decelerate climate change [34]. For these reasons the trapping mechanisms of supercritical $CO_2$ in geological structures of deep saline aquifers will be further explained in the upcoming part to later also give insight into how simulations and experiments can be conducted to get even deeper knowledge of the behavior of the flow.

Since the pore spaces and cavities of the storage structures are filled with fluid when $CO_2$ is first injected, it displaces present fluid and heightens reservoir pressure [34]. At standard atmospheric conditions $CO_2$ has a density of $1.9kg/m^3$ while at its supercritical conditions $\rho = 250 - 800kg/m^3$. The exact value depends on pressure gradients and temperature [2]. Viscosity and therefore its gas-like properties are on the other hand barely changing at all in the supercritical state. This means that the supercritical liquid $CO_2$ will spread the entire available volume like a gas [3]. Meanwhile, brine has a density of about $700 - 1200kg/m^3$ [6, 27]. The lower density of the $CO_2$ makes it buoyant and no matter where exactly in the reservoir the injection point is, the $CO_2$ will rise up through the formation fluid in the aquifer. Gravity currents, injection pressure and natural flow inside the aquifers introduce additional motion [4, 34]. This is why even with velocities as small as cm/year [4] ultimately there has to be a - as before mentioned - non-permeable layer that will physically stop the upward migration. Suppressing uprising motion, the $CO_2$ will still spread sideways into unknown terrain with eventual fractures or abandoned wells [17, 34]. Therefore, the caprock optimally has a downwards oriented concave shape not only restricting the ascending flow but also the lateral one [50] (see Fig. 1.1).

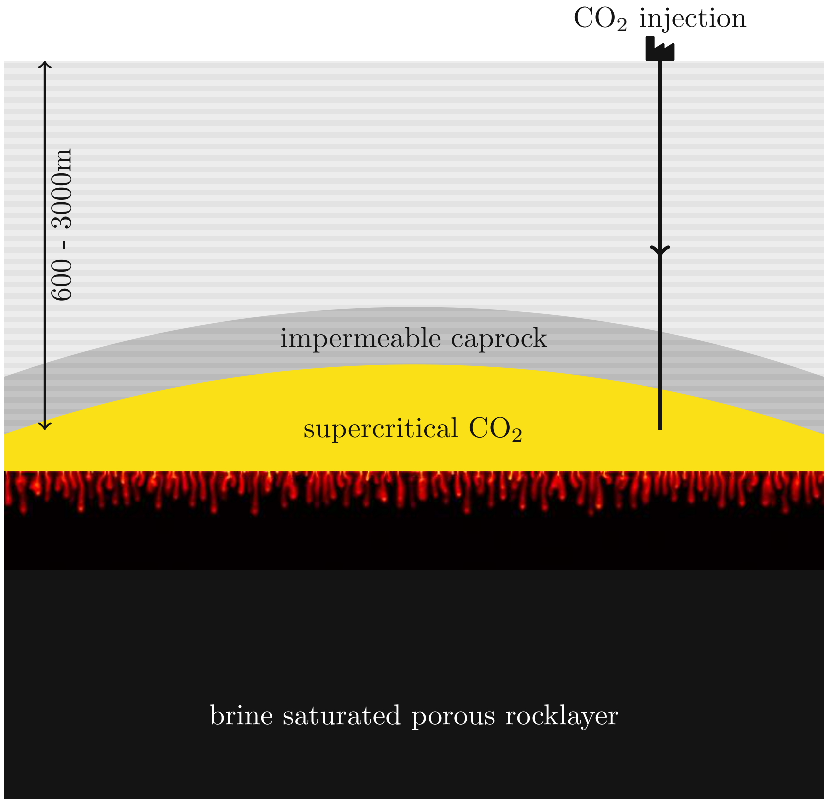

Figure 1.1 – Schematic of Carbon Dioxide Capture and Sequestration - CCS

The $CO_2$ might be physically trapped underneath the caprock but remains mobile and buoyant there [7]. This explains the before expressed need for a caprock without faults since uprising through cracks or abandoned wells happens readily. But even a, at the time of injection, non-faulty caprock can get cracks due to seismic activity or an elevated pressure inside the aquifer when too much $CO_2$ was injected. It generally is desirable to trap as much of the mobile $CO_2$ as possible additionally through non-structural trapping making storage more stable [7, 17, 34]. Mechanisms of non-structural trapping are capillary or residual trapping and the chemical securing mechanisms of solubility and mineral trapping, which will be explained in brevity in the next section.

Capillary trapping happens during the migration flow through the aquifer when the $CO_2$ displaces brine in the pores. When it does not stay stationary but moves further on, some residual - hence the name residual trapping - $CO_2$ stays trapped inside the pore spaces due to the backflow of brine which pushes it back inside the capillaries. However, that is not the main trapping mechanism [7].

Only when migration is stopped by the caprock where the $CO_2$ is trapped the major capture process, the solubility trapping begins. The carbon dioxide starts to gradually dissolve into the underlying brine forming an aqueous solution rich in $CO_2$. The solubility of liquid $CO_2$ into water is rather low, reducing further with increasing temperatures and amount of salt in the brine [6]. Nevertheless, a small amount of 3–5 $weight\%$ of supercritical carbon dioxide does mix with the brine [51]. This mixing results in the formation of a diffusive boundary layer on top of the brine with a density not only higher than the supercritical $CO_2$ but also than the resident fluid. This density difference of about 1 % is only very slight, but enough to induce further mixing [6, 34]. The layer of saturated brine grows through diffusion until it has sufficient thickness to become unstable and propels a downward motion of the denser fluid [18, 46]. The more $CO_2$ dissolves in that way, the lower is the risk of leakage, since it sinks instead of rising to possible leaks in the caprock [7, 17]. Through this process of dissolution over several thousand years, a quite reasonable amount of $CO_2$ can get trapped while ensuring storage security [34].

As almost a side effect of the carbon dioxide dissolution into the brine, the mineral trapping occurs. The aqueous solution of $CO_2$ and salt water forms carbonate and bicarbonate ions, so a weak carbonic acid, which results in a reduced pH of the solution. When these ions react with minerals inside the structure, solid carbonates can be the result [6]. It can be regarded as the most stable and secure form of capture [22]. For that to happen the formation not only needs to exhibit the before discussed properties but should also have calcium and magnesium which is present in sandstone and carbonates. Times needed for the binding of significant amounts of $CO_2$ lie at hundreds to thousands of years even in optimal aquifers [7, 17]. Another very permanent trapping mechanism is the adsorption of $CO_2$ unto the surface of organic materials contained in coals and shales, to which it exhibits a natural affinity [6]. Mineral trapping is especially effective in combination with the before described solubility trapping since the convective flow transports the solution to further areas of the aquifer, enhancing the capture as carbonates. It also unsettles the solutal trapping mechanism by the chemical reactions, thereby increasing dissolution flux and accelerating mass transport [7]. Still, considering the huge timescales needed it also plays a rather small part in non-structural trapping, making solubility trapping the most important capture mechanism, transporting the buoyant $CO_2$ further down away from possibly contaminating reservoirs nearer to the surface or in the worst case the surface itself.

Even with all these seemingly promising features for CCS, predictions on timescales, safety and storage capacity are still absolutely necessary. They can be performed with computer simulations. The next paragraph addresses the main simplifications and assumptions made for the successful implementation of CFD simulations. Different configurations have been modelled in these simulations, firstly in two dimensions and then also expanding them to three dimensions. The most examined is the Rayleigh-Bénard (RB) configuration, e.g. by Pirozzoli et al. [43]. The domain only contains one fluid and is cooled at the top boundary and heated from the bottom, thereby introducing a density gradient through temperature differences. There also is the Rayleigh-Taylor configuration in which the heavier fluid initially lies on top of the lighter one, initiating convective flow due to concentration-induced density differences (see e.g. [13]). Lastly there is the one-sided configuration which models the before described case of liquid $CO_2$ on top of pore space saturated with brine by prescribing a constant concentration at the top boundary of the heavier fluid with a density difference again based on concentration differences (see e.g. [48]).

Domains in the one-sided configuration are only including the porous layer and represent the carbon dioxide layer as a fixed $CO_2$ concentration on the top boundary thereby ignoring gravity currents under the caprock and assuming a stationary layer of liquid $CO_2$. This is legitimate since convection is very slow, compared to lateral migration, so it can be assumed that movement has ceased before dissolution begins [17]. A further simplification is the presumption of a sharp interface at that boundary between liquid $CO_2$ and brine. That ignores the actually present transition zone due to capillarity [17]. Due to the differences in liquids when injecting $CO_2$ into brine saturated aquifers the occurring problem is strictly speaking a two-phase flow problem. The lesser density of the $CO_2$ results in strong buoyant segregation, justifying the simplification of equations to a one-phase flow while still giving valuable insights into the process [6]. Regarding the lateral extension of the domain, different configurations have been tried out. First there is the option of considering an infinite lateral extension as done by Riaz et al. [46]. Pau et al. [40] and Hidalgo et al. [28] used periodic repetition of the lateral extension and lastly there is the possibility of a domain at all sides closed as no-flow boundaries as deployed by Hewitt et al., Neufeld et al., Riaz et al. and Slim [25, 36, 46, 48].

These simulations have been validated with small-scale experiments in the case of solubility trapping whereas the simulation of the thousands of years lasting mineralization is more difficult to reproduce in experiments. Experiments have been conducted in bead packs (e.g. [36]) as well as in Hele-Shaw cells (e.g. [49]). In the first case there is a domain filled with non-deformable beads that are transparent to make flow patterns visible. The latter one is two transparent plates arranged parallel to each other with only a small gap between them. At low fluid velocities inside the gap the flow behavior is comparable to flow in porous media described by Darcy's law [9]. To make patterns in the flux visible some worked with making pH differences perceptible while others used different analog fluids which are visible due to differences in transmitted light intensity (e.g. [25]) [7].

To additionally back up simulation results and get an even better insight, the CCS projects already in practice can be looked at. The most known one is the Sleipner CCS project where sequestration is conducted into the Utsira aquifer under the North Sea. There are other ongoing projects e.g. the In Salah project as well, but the annual injection rate in all of them together is still lower than the output of one large coal-fired power plant [6]. Still, evaluation of aquifers, capacity estimates and key monitoring insights can be gained by these trial projects.

The just presented research - might it be simulations or actual injection of $CO_2$ into the ground - supports the expectation of occurring convection at most sequestration sites [36] which is a good first step but extending simulations and experiments are to be supported.

In this work, further simulations in the two-dimensional one-sided configuration have been conducted with a newly adjusted computational code. Objective was the description of flow dynamics to understand solute transport and sizes of emerging flow structures, comparison of mixing measures and comparison of different aquifer sizes corresponding to different Rayleigh Darcy numbers. The results were also compared to existing research to make sure of the correctness in computation and usability of the adjusted code. In the next chapter, details to the used model and numerical methods as well as an overview over the carried out simulations is given. The chapter after that which contains the simulation results is divided in the following way. First, the general flow field at different time stages is examined to talk about flow structure sizes and flow development. That leads into the identification of the time dependent flow regimes.

After that an introduction to the measures of mixing is given to end the chapter with a comparison between different Rayleigh Darcy numbers. Lastly, there is a conclusion summarizing the found results and giving ideas for further possible advancement of research.

# 2

# Methodology

## 2.1 Model

To model the described problem in a way that still makes it computationally feasible, some approximations must be introduced. In this work, a two-dimensional (2D) fluid-saturated porous medium with uniform permeability $\kappa$ and porosity $\phi$ is assumed. The layer has a fixed vertical extension of one (in dimensionless units) in the y-direction and variable lateral extension with periodic boundary conditions in the horizontal x-direction. The walls are considered as impermeable and isothermal. Gravity acceleration $g$ is directed in the negative y-direction. Initially, the medium is filled with pure brine ($C(x, t = 0) = 0$). On top of the saturated brine layer, there is a large layer of $CO_2$, characterized by uniform and constant $CO_2$ concentration. The fact that the layer of $CO_2$ has constant and uniform concentration is reasonable since the convective processes are very slow and gravity currents underneath the caprock are being ignored, so it can be assumed that at the time of the simulation the movement of the $CO_2$ has stopped and the saturatisation of the local brine is stabilized before convection begins [17]. This layer is described by the application of a fixed concentration of $C_{top} = -1$ at the top boundary. The interface between the $CO_2$ layer and the porous medium is sharp and undeformable. This density difference between the top boundary and the interior of the domain is unstable and induces the start of the flow development.

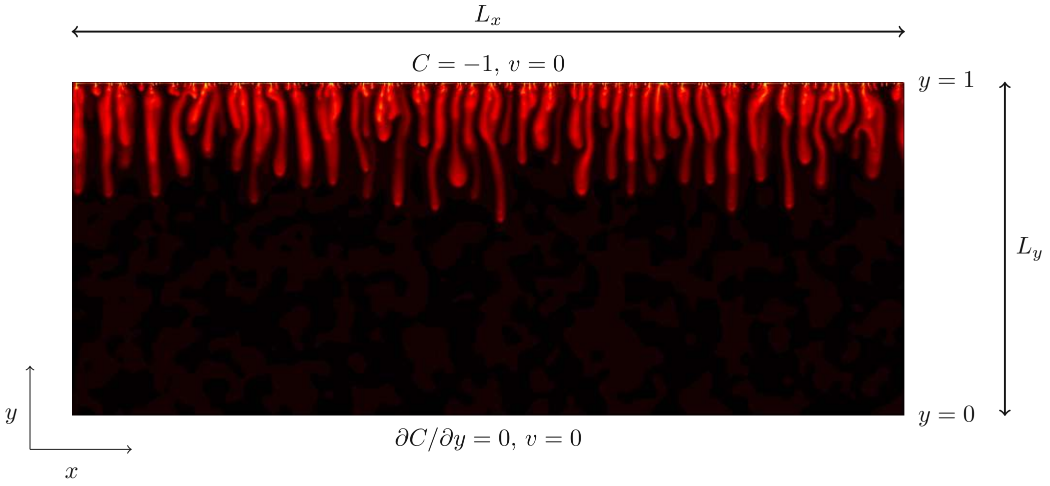

Figure 2.1 – Sketch of the modelled domain

### 2.1.1 Governing Equations

#### Dimensional Equations

The equations describing flow in a porous layer are described in the following. Dimensional variables are indicated with a $*$ superscript. The Oberbeck-Bossineq approximation is valid [53] and the flow is considered as incompressible.
The continuity equation reduces to

$$\nabla \cdot \boldsymbol{u}^{*} = 0 \tag{2.1}$$

due to the assumed incompressibility of the fluid with $\mathbf{u}^{*} = (u^{*}, v^{*}, w^{*})$ being the volume averaged velocity field. The inertialess flow in porous media is described by Darcy's law as

$$\boldsymbol{u}^{*} = -\frac{\kappa}{\mu}[\nabla p^{*} - \rho^{*}(C^{*}) g \boldsymbol{j}] \tag{2.2}$$

with $\mu$, the fluid viscosity and $\kappa$, the permeability which both are constant, $p^{*}$ the pressure, density $\rho^{*}$ in dependence of the concentration $C^{*}$ and $\boldsymbol{j}$ the unit vector in vertical direction. The advection-diffusion equation

$$\phi \frac{\partial C^{*}}{\partial t^{*}} + \nabla \cdot (\boldsymbol{u}^{*} C^{*} - \phi D \nabla C^{*}) = 0 \tag{2.3}$$

describes the redistribution of the solute. Note that, $t^{*}$ is the time, $D$ is the diffusivity, considered as constant, while $\rho^{*}$ is the fluid density, expressed as a linear function of the concentration field $C^*$

$$\rho^*(C^*) = \rho^*(C^*_{min}) - \Delta\rho^* \frac{C^* - C^*_{min}}{C^*_{max} - C^*_{min}} \tag{2.4}$$

with $\Delta\rho^* = \rho^*(C^*_{min}) - \rho^*(C^*_{max})$.

### Dimensionless Equations

A natural velocity for the system is the buoyancy velocity, the speed with which a fully saturated fluid parcel falls $V^* = g\Delta\rho^*\kappa/\mu$. A length scale can be chosen as the height of the domain $h^*$. Upon introduction of the dimensionless variables

$$C = \frac{C^* - C^*_{min}}{C^*_{max} - C^*_{min}}, \quad t = \frac{t^*}{\phi h^*/V^*}, \quad p = \frac{p^*}{\Delta\rho^* g h^*}, \tag{2.5a-c}$$

(2.5a)

the governing equations reduce to their dimensionless forms

$$\nabla \cdot \boldsymbol{u} = 0, \tag{2.6}$$

$$\boldsymbol{u} = -\frac{1}{\mu(C)}[\nabla p - \rho(C)\boldsymbol{y}], \tag{2.7}$$

$$\partial_t C + \nabla \cdot (\boldsymbol{u}C - \frac{1}{Ra}\nabla C) = 0. \tag{2.8}$$

The single non-dimensional parameter in the system, the Rayleigh-Darcy number, reads as

$$Ra = \frac{V^*H^*}{\phi D} = \frac{\kappa\Delta\rho g H^*}{\mu\phi D} \quad . \tag{2.9}$$

where, as anticipated above, $H$ represents a typical length scale of the problem (the height of the aquifer in this case), $V^*$ is the so-called buoyancy velocity which is a natural reference velocity scale [19, 52]. The Rayleigh Darcy number is generally associated with buoyancy driven flow and characterizes the ratio of driving buoyancy forces to diffusive forces [17]. It is therefore a control parameter for the initiation of convection, where no convective flow appears for $Ra < 4\pi^2$ [30]. With a higher Rayleigh Darcy number, the flow becomes more and more turbulent and advective transport mechanisms dominate over diffusive ones.

The dimensionless wall boundary conditions are

$$v(y=0)=0, \quad C(y=0)=0 \tag{2.10a}$$

$$v(y=1)=0, \quad C(y=1)=-1 \tag{2.10b}$$

also indicated in Fig. 2.1.

## 2.2 Numerical Methods

The numerical computations are centered around a by Pirozzoli et al. [43] already used code for the two-sided Rayleigh–Bénard (RB) configuration to the problem. The existing source code was adapted for the one-sided configuration. It is a second-order finite-difference incompressible flow solver which is based on the staggered arrangement of the flow variables [37]. In a staggered grid which was introduced by Harlow et al. [23] scalar variables like pressure are stored in the cell centers while velocity variables are saved at the cell boundaries. This is done to avoid a discretization error called odd-even decoupling, which represents one of the main complications in simulating incompressible flows. When central differences are used to compute derivatives, only every second point on the grid is connected, which leads to convergence problems of the computation when using collocated grids [45]. The utilized code has been used and proven correct and reliable for Direct Numerical Simulation (DNS) by Pirozzoli et al. [41, 42] for wall-bounded neutrally-buoyant and unstably-stratified turbulent flows and as just mentioned for convective dissolution flows in a RB cell [43].

Advancement of the solute transport equation in time is achieved through a hybrid third-order low-storage Runge-Kutta algorithm. The convective terms are computed explicitly whereas the diffusive terms are handled implicitly, limited to the vertical direction. Like that, in the limit of inviscid flow, the total concentration variance is preserved in a discrete way.

To handle the pressure term in the momentum equation that for the reason of incompressibility does not appear in the continuity equation, the Poisson equation can be decoupled for the pressure with the divergence-free constraint,

$$\nabla^2 p = \frac{\partial C}{\partial y}, \tag{2.11}$$

with $\partial p/\partial y = 0$ at the top and bottom boundary to satisfy the impermeability condition. The pressure field is thus calculated in a way that the rate of change of the velocity variance disappears everywhere and therefore needs the solution of the Poisson equation attained by relaxation or another procedure [23].

This equation is then fed into the equations of state to then Fourier expand them in the horizontal periodic directions. The result is a system of tri-diagonal equations in the wall-normal direction for each Fourier mode that can be solved with standard numerical techniques [32, 37].

The mesh spacing in the vertical direction, the direction of main flow, is based on the insights obtained in [43]. To better resolve the boundary layers near the walls, where gradients and flow dynamics are more significant, an error function stretching is applied to the before as uniform defined grid. This compresses the grid near the boundaries and expands it in the center of the domain. Like that a better resolution near the walls can be achieved while the middle with lesser gradients is resolved with fewer grid points therefore resulting in lower computational cost. In the horizontal direction x the grid spacing is uniform.

Timestepping is defined so that the (CFL) number is approximately unity for all performed simulations.

## 2.3 Assessment of grid resolution and domain size

### 2.3.1 Grid sensitivity study

To understand the influence of the grid size on the results, a mesh sensitivity study has to be performed [47]. This means that the same simulation is run on different resolutions and the results are then compared [20]. The aim is always to identify a mesh which is fine enough so that it can display all the important information but results in the minimum computational cost. In this case, to compare the different meshes, two quantities were considered that were already used in past research so to be able to compare results and see convergence with changing resolution. The measures are the mean dissolution flux $\langle F \rangle_t$ and the mean wavenumber $\langle k \rangle_{x,t}$ near the top boundary of the domain averaged over a certain timespan (i.e. $2 \cdot 10^4 < t < 15 \cdot Ra$). More on what exactly these measures are and how they get computed will follow later, while here the focus lies on the choice of grid. As established before, the verification of the code for the same class of problems has already been done in the past, and it can be assumed that changes in results are only a reason of the changing grid resolution.

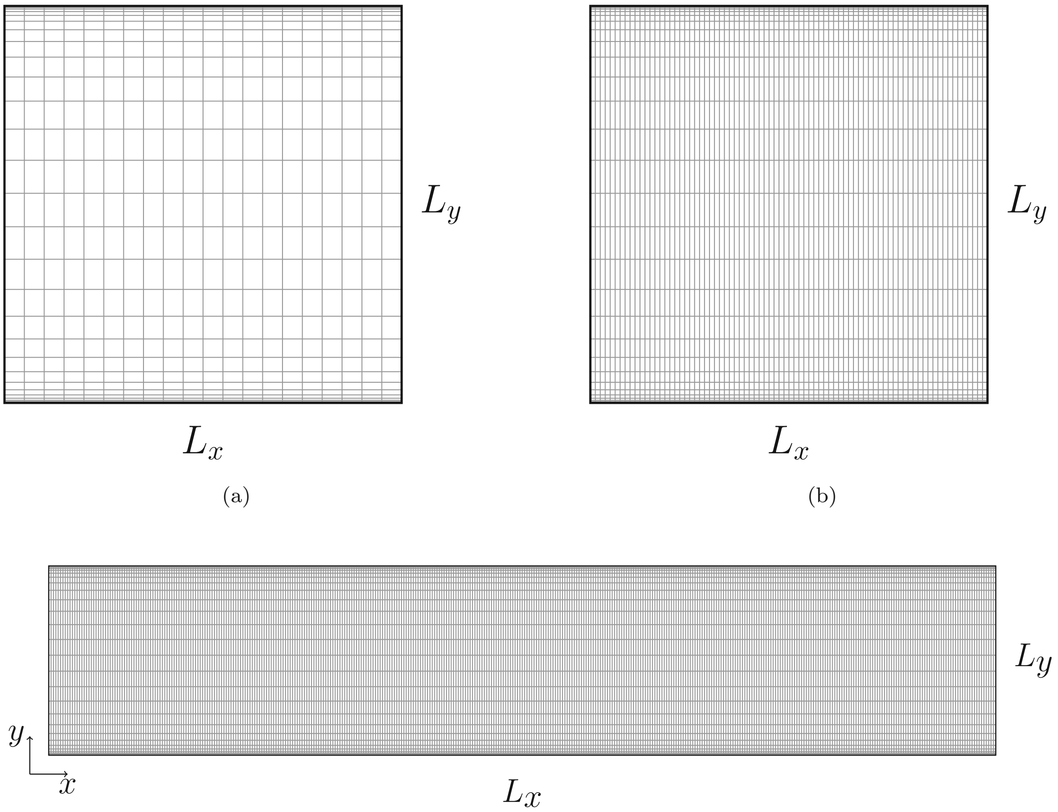

(a)

(b)

(c)

Figure 2.2 – Different grid resolutions on different domain sizes. The upper part shows quadratic domains ($L_x = L_y = 1$) with (a) a grid with an equal number of points in both directions ($N_x = N_y$) to start the grid assessment. Secondly, (b) shows a grid with an unequal number of points ($N_x > N_y$). (c) shows the change in domain size to a larger width, here resulting in an aspect ratio of $AR = L_x/L_y = 5$ to investigate influences of the domain width.

To perform the grid sensitivity study, first the 1x1 domain was looked at. This means choosing $L_x = L_y$, resulting in a quadratic area, as can be seen in the upper part of Fig. 2.2. In that figure, the stretched grid and variations in resolution and domain size are shown to better explain the procedure of the assessment. Fig. 2.2 (a) shows an arbitrarily chosen resolution with equal number of points in both spatial directions, $N_y = 128$ and $N_x = 128$. This is the configuration the evaluation is started with. For clarity not all points are displayed in the figure but an adjusted smaller number. The process is advanced by raising the number of points in x-direction while keeping the number of points in y-direction the same. In Fig. 2.2 (b), such a grid with a different number of points for the different spatial directions in shown. $N_x$ was doubled until $N_x = 2048$, resulting in five simulations to consider, and the addressed quantities used to compare were recorded.

To decide on a value for the number of points the values of $\langle F \rangle_t$ and $\langle k \rangle_{x,t}$ are plotted over the different resolutions $\Delta x$ in Fig. 2.3. The value of $\langle F \rangle_t$ - as seen in (a) - fluctuates with a decrease of the resolution, until $N_x = 1024$ or $\Delta x = 0.00098$ and does not seem to change anymore with a further elevation of grid points. What additionally speaks for that number of grid points is the proximity of the $\langle F \rangle_t$-value to 0.017 which was introduced by past research and is indicated by the dashed line in the plot. Also $\langle k \rangle_{x,t}$ - as seen in (b) - appears to reach some kind of steady range with $N_x = 1024$. This resolution for x, indicated by a red dot, is therefore chosen to be appropriate for the extent of this work.

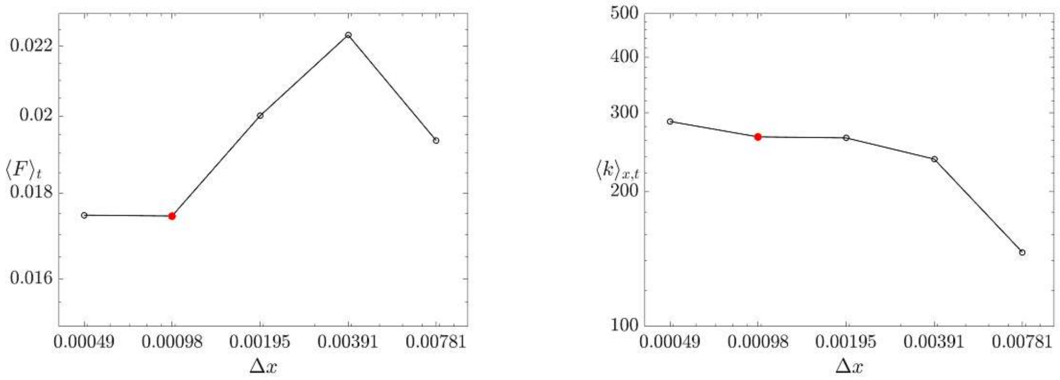

(a) (b)

Figure 2.3 – Effect of grid refinement in x-direction on (a) mean flux $\langle F \rangle_t$ and (b) mean wavenumber $\langle k \rangle_{x,t}$. The dashed line in the left plot is marking the expected value of $\langle F \rangle_t$. The red dot marks the for this work, chosen resolution of $N_x = 1024$.

To decide on the number of points in y-direction the same procedure was followed, doubling $N_y$ starting from 64 up to a number of 512, resulting in four simulations to assess. Again, values of $\langle F \rangle_t$ and $\langle k \rangle_{x,t}$ are evaluated and the decision process of choosing the resolution is shown in Fig. 2.4 where the values are plotted over $\Delta y$ now. In opposition to $N_x$, the number of points in y-direction do not seem to have as big an influence on both $\langle F \rangle_t$ and $\langle k \rangle_{x,t}$. Big changes in value do not occur even at low resolutions, suggesting that a low number of grid points in y-direction is good enough.

With the reduction of $N_y$ the value of $\langle F \rangle_t$ however draws closer to the aforementioned postulated value of 0.017. Based on that insight and to still ensure a proper resolution in this direction of main flow, $N_y = 256$ or $\Delta y = 0.0039$ was chosen, as indicated in the figure by the red dot.

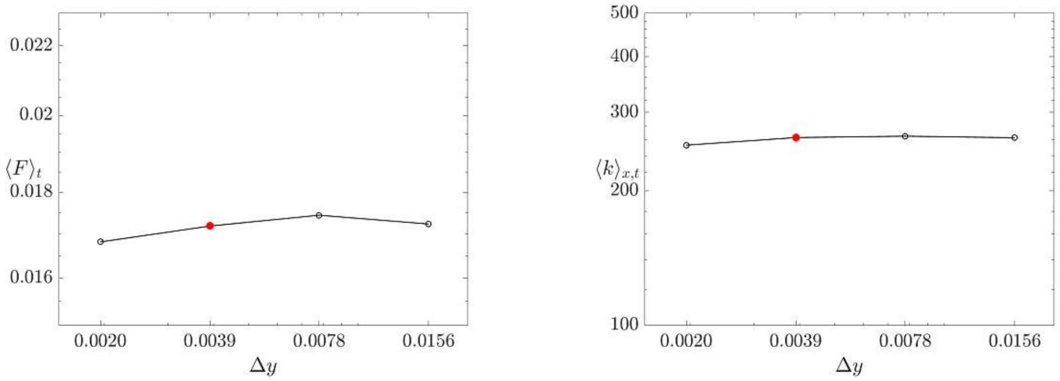

(a) (b)

Figure 2.4 – Effect of grid refinement in y-direction on (a) mean flux $\langle F \rangle_t$ and (b) mean wavenumber $\langle k \rangle_{x,t}$. The dashed line again shows the expected value of 0.017 and the red dot marks the chosen resolution of $N_y = 256$.

### 2.3.2 Boundary effects

To find out about the effects that the periodic boundary conditions have on the flow, additional simulations were performed in which the computational domain widths were varied (recorded in Table 2.1). As mentioned, length and width are equal ($L_x = L_y = 1$ ) for the first part of the assessment (seen in the upper part ((a) and (b) of Fig. 2.2). For the next part of the evaluation the width $L_x$ is enlarged, exemplarily to a value of five in the lower part of Fig. 2.2. With a change of the width, the ratio $L_x/L_y$, titled aspect ratio, $AR$ changes also and is used from now on to indicate a non-quadratic simulation domain (when $AR \neq 1$). Like in the grid sensitivity assessment, the goal is to use the smallest possible width with no influences by the boundary effects, to keep computational cost low. Considering aspect ratios up to 20 the dissolution flux as well as the wavenumber near the top wall were averaged over time to be regarded in the decision-making. Throughout the variation of the domain width, the resolution is always kept the same by adjusting the number of points in x-direction. Fig. 2.5 shows the recorded values of $\langle F \rangle_t$ in (a) and $\langle k \rangle_{x,t}$ in (b) plotted against $AR$. While the values of $\langle F \rangle_t$ do not seem to be influenced a lot by the aspect ratio, staying around

| $N_x \times N_y$ | $AR$ | $\langle F\rangle_t$ | $\langle F\rangle_t^{MM}$ | $\sigma/10^{-4}$ | $\sigma_{MM}/10^{-4}$ |
|---|---|---|---|---|---|
| $512 \times 256$ | 0.5 | 0.01803018 | 0.01773976 | 15.28 | 10.14 |
| $1024 \times 256$ | 1.0 | 0.01718291 | 0.01726868 | 9.05 | 4.85 |
| $2048 \times 256$ | 2.0 | 0.01686012 | 0.01685691 | 4.35 | 1.75 |
| $5120 \times 256$ | 5.0 | 0.01712661 | 0.0171062 | 4.04 | 1.42 |
| $10240 \times 256$ | 10.0 | 0.0170068 | 0.01699609 | 4.43 | 1.96 |
| $20480 \times 256$ | 20.0 | 0.0170068 | 0.01699609 | 4.43 | 1.96 |

Table 2.1 – Effect of the domain size (horizontal aspect ratio, $AR = L_x/L_y$) on the flow at $Ra = 1 \times 10^4$. Different aspect ratios in the range $0.5 \leq AR \leq 20.0$ are considered while keeping the resolution constant. Mean flux, averaged over the whole timespan ($\langle F\rangle_t$) and calculated with a running average ($\langle F\rangle_t^{MM}$, window size for the running average was taken as 1/4 of the recorded points during the looked at time span) as well as their fluctuations $\sigma$ are stated.

the value of 0.017, the mean wavenumber shows a stronger dependence. The mean flux really only shows a deviation when choosing $AR$ smaller than 1. Values of $\langle k\rangle_{x,t}$ on the other hand rise with a higher $AR$. From this, it is admittedly not that easy to decide on a suitable aspect ratio, which is why additional measures were looked at. These are recorded in table 2.1 and entail the mean flux additionally calculated with a running average $\langle F\rangle_t^{MM}$ and the fluctuations $\sigma$ of the flux, first for the conventionally calculated mean flux and then as well for the moving-mean-flux. It is observable there that using a moving average does not make a big difference in values when compared to averaging over the whole timespan. Fluctuations, however, give a better measure on choosing the $AR$ as they decline significantly with bigger domain width. This is in alignment with the results of De Paoli et al. [14] where it was shown that shrinkage of the domain results in a confinement of flow structures, meaning the fingers are missing space to develop properly. Also, the aforementioned increase of $\langle k\rangle_{x,t}$ with increased $AR$ supports the previous statement, since the wavenumber is proportional to the inverse of the length scale, therefore giving an idea of flow structure size. Only for an aspect ratio of five or higher, the mean wavenumber stays at a constant value, indicating an independence from domain size. That is why ultimately an aspect ratio of five was chosen for the simulation at $Ra = 1 \times 10^4$.

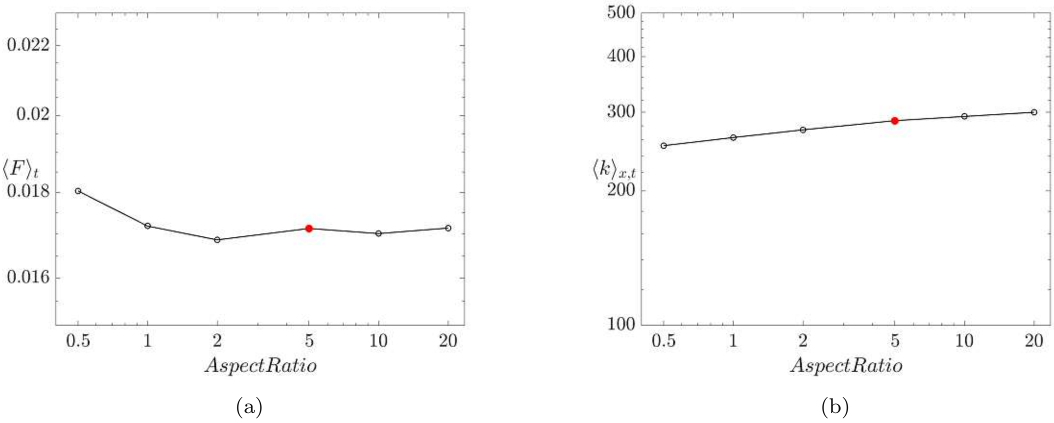

(a)

(b)

Figure 2.5 – Effect of domain width on (a) mean flux $\langle F\rangle_t$ and (b) mean wavenumber $\langle k\rangle_{x,t}$. The aspect ratio used in this work - $AR = 5$ - is indicated by the red dot.

## 2.4 Computational Details

To simulate different aquifer sizes, the before introduced Rayleigh-Darcy number can be varied. In this section, the details of the performed simulations will now be described shortly. For the different $Ra$ numbers, the results of the assessments on resolution and domain width were up or down scaled proportionally to arrive at the simulation parameters shown in table 2.2. Thereby, the number of points $N_x$ and domain width $L_x$ were chosen so the resolution $\Delta x = L_x Ra/N_x$ is kept at the same value of 9.7656 throughout all the simulations. The number of points in y-direction, $N_y$ are also adjusted according to the value of $Ra$.

| Simulation | $Ra$ | $N_x \times N_y \times N_z$ | $L_x : L_y$ | $F_{mean}$ |
|---|---|---|---|---|
| $S_{100}$ | $1 \times 10^2$ | $256 \times 16 \times 1$ | 25 | - |
| $S_{200}$ | $2 \times 10^2$ | $512 \times 24 \times 1$ | 25 | - |
| $S_{500}$ | $5 \times 10^2$ | $1280 \times 32 \times 1$ | 25 | - |
| $S_{1000}$ | $1 \times 10^3$ | $2560 \times 48 \times 1$ | 25 | - |
| $S_{2000}$ | $2 \times 10^3$ | $5120 \times 64 \times 1$ | 25 | 0.0171337 |
| $S_{5000}$ | $5 \times 10^3$ | $5120 \times 128 \times 1$ | 10 | 0.0167257 |
| $S_{10000}$ | $1 \times 10^4$ | $5120 \times 256 \times 1$ | 5 | 0.0170890 |
| $S_{20000}$ | $2 \times 10^4$ | $5120 \times 512 \times 1$ | 2.5 | 0.0168825 |
| $S_{40000}$ | $4 \times 10^4$ | $5120 \times 1024 \times 1$ | 1.25 | 0.0171558 |
| $S_{60000}$ | $6 \times 10^4$ | $5120 \times 1024 \times 1$ | 0.625 | 0.0171558 |

Table 2.2 – Details of the simulation parameters for the performed simulations. In the last column the mean flux during the constant flux regime from $2 \cdot 10^4 < t < 15 \cdot Ra$ is displayed.

**Initial condition** Convection starts when the diffusive layer at the top boundary becomes so thick that it becomes gravitationally unstable [48]. To simulate this instability, random noise is added to the concentration field at the start of the simulation at $t_0$ as

$$C = -1 + \mathrm{erf}\left(\frac{1-y}{h_{initial}}\right) \cdot (1 + 0.01(a - 0.5)) \quad . \tag{2.12}$$

$a$ is a randomly generated number between 0 and 1 and $h_{initial}$ is the initial thickness of the diffusive layer, which is defined as dependent on Rayleigh

$$h_{initial} = 2\frac{\sqrt{t_0}}{Ra} \quad , \tag{2.13}$$

with $t_0 = 250$.

As the final time for the simulations, usually $t_{conv} = 100$ was chosen. This ensures the passing through all the important stages of the flow dynamics but does not take up too much computational time. Only some individual simulations were run for longer to obtain a further understanding of the very late stages of the problem.

The general timestepping that is subject to the CFL condition needs to get adjusted for time intervals where velocities are very low. Due to these small velocities the implemented timestepping condition calculates the timesteps as much too big which results in strong fluctuations in the behaviour of the results. Additional timestep limitations during the beginning and end stages of the computation are introduced to avoid these imprecise outputs. In Fig. 2.6 the timesteps $dt$ of a simulation with and without timestep limitations at the end is shown. The unadjusted case is the black line. $dt$ increases more and more at later times and also starts to exhibit fluctuations which both influences the results in a unfavorable way. When a limitation is introduced - depicted by the light blue curve - the applied condition takes effect, keeping $dt$ at a constant lower value.

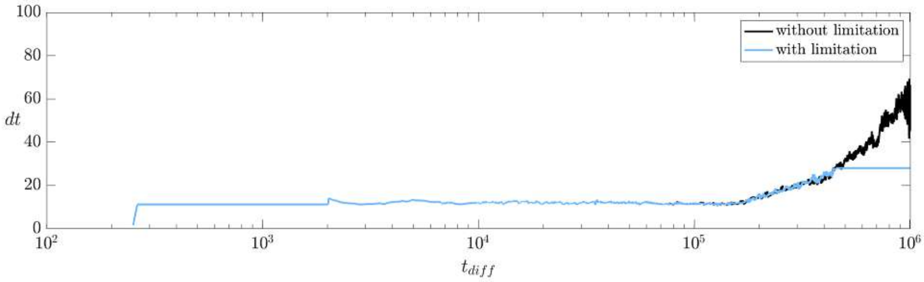

Figure 2.6 – Time behavior of the timesteps for the simulation $\mathrm{S}_{10000}$ at $Ra = 1 \times 10^4$ to compare an introduced timestep limitation with the behaviour when no limitation is applied.

# 3

# Results

In this chapter, the results of the performed numerical simulations are discussed and compared to former results. The first part of this chapter will entail a discussion of the general visual appearance of the flow and its structures sizes. Afterward, the time-dependent process will get categorized into different stages. Trends of measures in these regimes have already been modelled, in that part of the work the match with these proposed models are also investigated. After that, the different measures of mixing are addressed and their behavior with time are compared to each other. To conclude the chapter, the influence of the Rayleigh Darcy number on the process is observed.
The simulation at $Ra = 1 \times 10^4$ was chosen to analyze the time-dependent flow field dynamics and will be used in the following sections as the reference when no comparison with other Rayleigh Darcy numbers is conducted.

## 3.1 Flow Field Visualization and Flow Structures

### 3.1.1 Flow Field

To understand the flow field and its structures in the left column of Fig. 3.1 the development in time of the flow field is visualized. Each panel corresponds to a different time step, using diffusive units. The color black represents areas with a $CO_2$ concentration of zero, whereas areas that are yellow represent the highest possible concentration of -1. The developments are also well visible in the profiles of the horizontally averaged concentration and vertical velocity variance in the middle and right columns. They are plotted so the y-axis corresponds to the height of the domain and is therefore in the same orientation as in the visualizations on the left, making the spatial variability of both measures observable. Horizontally averaged quantities are generally computed by

$$\langle a \rangle_x(y,t) = \frac{1}{W}\int_0^W a(x,y,t)dx \tag{3.1}$$

for any variable $a$. For the concentration Eq. 3.1 becomes

$$\langle C \rangle_x(y,t) = \frac{1}{W}\int_0^W C(x,y,t)dx \quad . \tag{3.2}$$

Since the mean vertical velocity, calculated with Eq. 3.1 from the global statistics is always zero due to the nature of the problem, one alternative way to discuss flow velocity is to use

$$\langle v'^2 \rangle_x = \langle v^2 \rangle_x - \langle v \rangle_x^2 \quad , \tag{3.3}$$

the variance of the vertical velocity. It can be regarded as the representative plume velocity corresponding well with the finger locations, giving insight into the spatial distribution of solutes within the porous medium and showing areas of enhanced mixing. The problem starts with the earlier introduced diffusive boundary layer with a fixed concentration of $CO_2$ at the top boundary and an empty rest of the domain with a concentration of zero throughout, which is visible in the first panel. After some time starting from that layer of constant concentration convective cells, called fingers or plumes, start forming as seen in panel two and three of Fig. 3.1. These fingers flow down in the direction of gravity into the empty domain. Corresponding to the length of the fingers (compare flow field visualization) the concentration and velocity variance profiles deviate from zero.

Ultimately they reach the bottom of the domain where they first spread laterally. That is why the denser fluid starts to accumulate and the porous medium gets filled up from the bottom by continuously following fluid with a higher concentration. This is well discernible by the fact that concentrations in the vicinity of the lower boundary are higher than in the middle of the domain. Concentration changes from zero at the lower boundary shortly after fingers impinge there. The more uniform the distribution of $CO_2$ in the aquifer, the straighter the concentration profile, which during late times just gets moved parallelly towards lower values of $\langle C \rangle_x$.

Until the end of the visualizations, finger like structures are visible even though they become more and more spread out with time, as seen in the visual progression of the

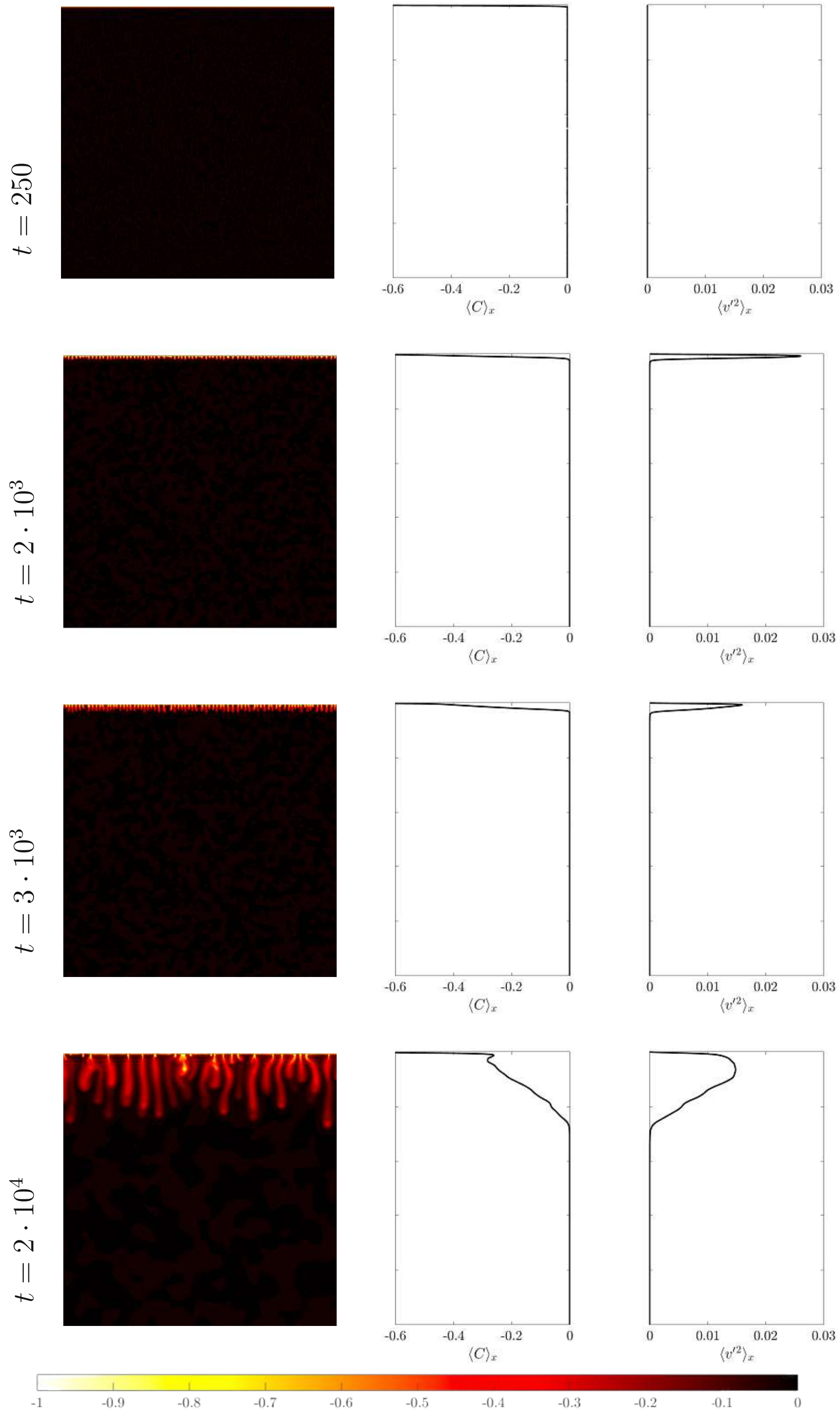

Figure 3.1 – Solute transport in a porous domain in 2D at aspect ratio $AR = 5$, at $Ra = 1 \times 10^4$. Left column: behavior of the solute concentration distribution shown on a quadratic section of the whole domain. Central column: average concentration profile, $\langle C \rangle_x$. Right column: velocity variance, $\langle v_y'^2 \rangle_x$. The plots in center and right are profiles averaged over the width of the domain and plotted over the height. Each row, from top to bottom, corresponds to a different, later time instant, as explicitly labelled.

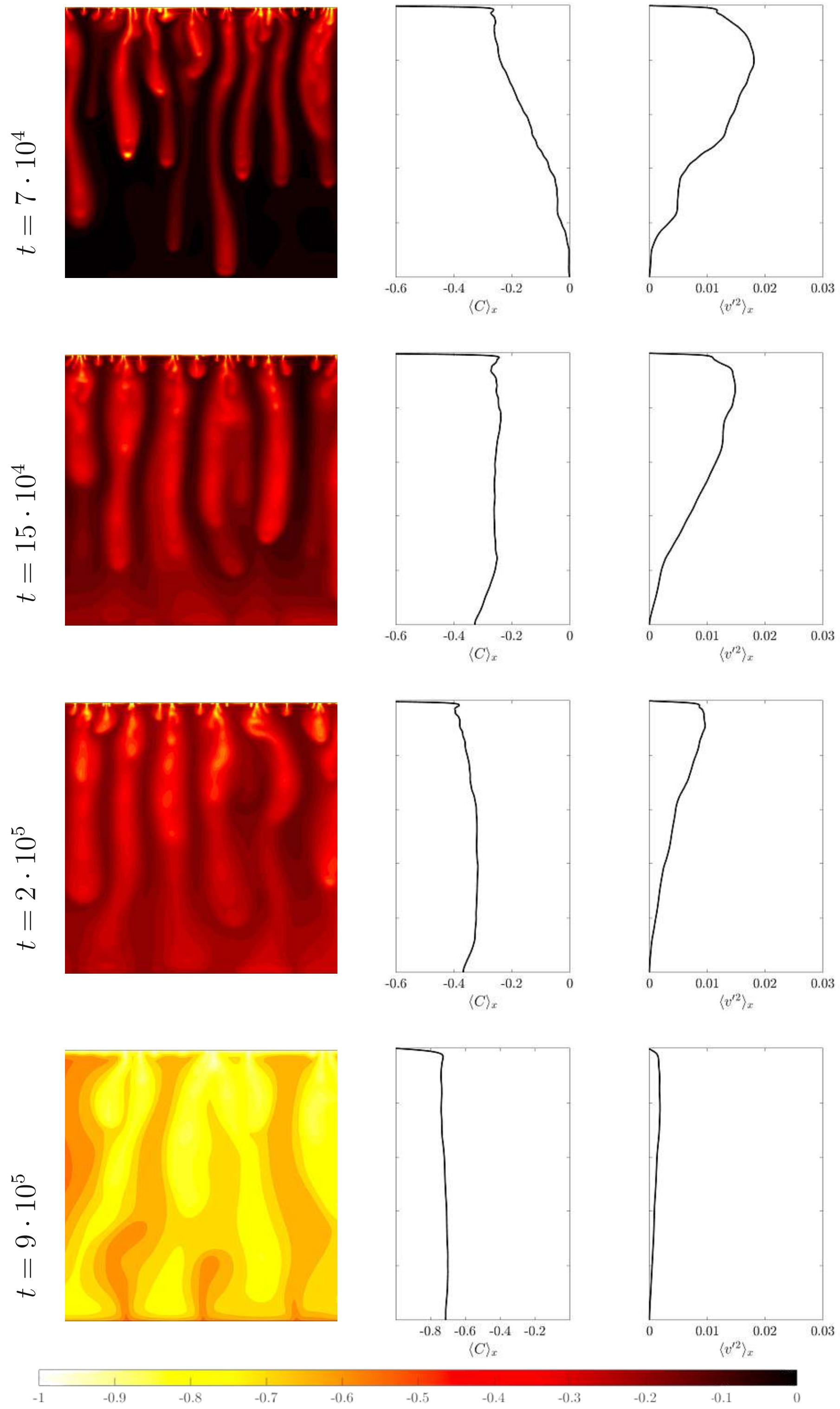

Figure 3.1 – Solute transport in a porous domain in 2D at aspect ratio $AR = 5$, at $Ra = 1 \times 10^4$. Left column: behavior of the solute concentration distribution shown on a quadratic section of the domain. Central column: average concentration profile, $\langle C \rangle_x$. Right column: velocity variance, $\langle v_y'^2 \rangle_x$. The plots in center and right are profiles averaged over the width of the domain and plotted over the height. Each row, from top to bottom, corresponds to a different, later time instant, as explicitly labelled.

last two panels. This suggests a decay of convection at later times also discernible by the decay of the velocity variance with time. Bigger values of $\langle v_y'^2 \rangle_x$ mean more pronounced and strongly advancing fingers. At the very end of the problem (not shown here) the convective fingers are not visible anymore and the domain holds an evenly mixed solution. The entire process of solute transport is characterized by complex dynamics, which will be described in more detail below (section 3.2).

### 3.1.2 Size of flow structures

To further investigate the flow field, the lateral structure of the flow will be considered, by looking at the average wavenumber $\langle k \rangle_x$ and the inverse of the wavenumber $\lambda = 2\pi/\langle k \rangle_x$ which corresponds to the size of the flow structures [43]. This does not mean the spacing between plumes but actually the width of a single plume as has been proposed by Slim [48] and coincides with the results found here. The wavenumbers are calculated by performing the Fourier transform of the concentration distribution at a certain height of the domain. By squaring the results of the Fourier transform, one derives the power spectrum density, $P$ which is then used to calculate

$$\langle k \rangle_x = \left\langle \frac{\int kP(k)dk}{\int P(k)dk} \right\rangle_x \quad , \tag{3.4}$$

the horizontally averaged wavenumber [26].

To quantify the development of flow structures in vertical direction, concentration distributions at three heights of the domain were considered in this work as indicated in the visualization on the right of Fig. 3.2: near the top boundary, in the middle of the domain and near the bottom wall. On the left of Fig. 3.2, values of lambda at different domain heights and times are depicted. Note that $\lambda$ is dimensionless and can reach values between 0 and 1. Looking at that, the change of plume width with height and time can be discussed. Near the top boundary, at $y = 1 - 50/Ra$ the flow structures are small since there the fingers have just formed and concentration gradients are much sharper than further down the domain. There, they also keep the same order of magnitude throughout the whole transient development of the flow. This is due to the nature of the boundary condition of constant concentration, supposing an endless amount of dissolvable $CO_2$. If that would not be the case, a change in value over time

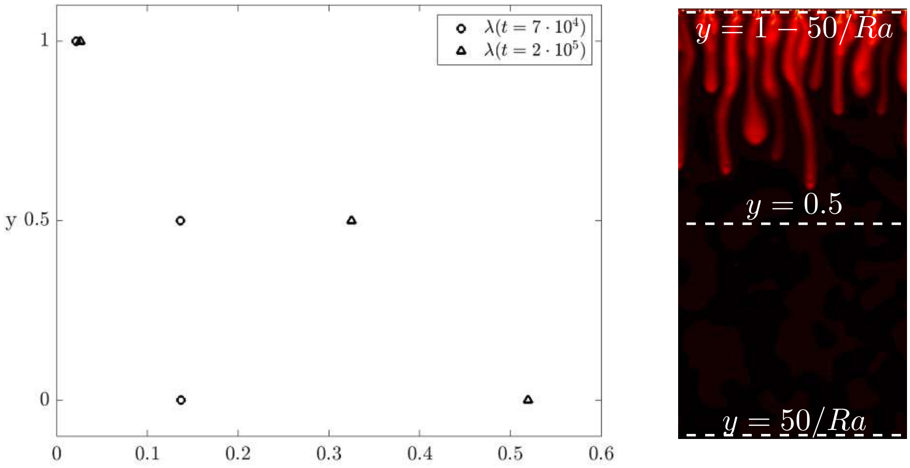

Figure 3.2 – The size of flow structures $\lambda$ at different heights of the domain at two points in time for the simulation at $Ra = 1 \times 10^4$. The heights are indicated as white dashed lines on the right visualization.

could be expected. At different heights inside the domain, fingers are not as pronounced as in the vicinity of the boundary, resulting in bigger values for $\lambda$. This means that as soon as fingers start flowing down, they also spread out. During the first part of the simulation, while plumes are flowing down unobstructed into an empty domain as seen in the flow field visualizations in Fig. 3.1 before, $\lambda$ does not change in magnitude from the middle to the bottom. At later times, structures get larger, especially at the bottom boundary. This corresponds to the lateral spreading of the plumes at the bottom, as discussed before in section 3.1.1. As also seen there, these enlarged structures then distribute from the bottom up throughout the domain: with time, values for $\lambda$ get bigger and bigger also at the middle of the domain, at $y = 0.5$.

These results agree well with the flow field visualizations in Fig. 3.1: Near the top boundary many small fingers with very high concentration (yellow in color) are discernible, not changing in number over time. In contrast, far from the top boundary, the plumes change considerably, which is especially well observable in the last panels.

This suggests convective flow during the first part of the simulation, characterized by higher values in velocity variance and smaller and more refined structure sizes; in later stages, diffusion starts to dominate again, supported by an increase in $\lambda$-values and a decrease in velocity. These findings propose a classification in different stages based on the dominant mechanisms of transport, which is done in the next section.

## 3.2 Identification of Flow Regimes

The time-dependent dynamics described above, apparent in the flow visualization, are also well visible in the time behavior of the dissolution flux, $F(t)$, which is plotted in Fig. 3.3 as a function of time. Note that time is expressed in diffusive units. The flux describes the flow from the diffusive boundary layer down into the rest of the domain and is evaluated at the top boundary as

$$F(t) = \frac{1}{Ra} \int_0^W \left. \frac{\partial C(x,y,t)}{\partial y} \right|_{y=1} dx \quad . \tag{3.5}$$

Based on the development of the flux, the problem can get categorized into three main stages [48]. First, there is a strong decline in the curve, which corresponds to diffusion-dominated mechanisms, customary for the first stage of the process. After an increase and another decline in value, the dissolution flux starts to fluctuate around a constant value. That is the so-called constant flux regime, which is strongly convection-dominated. At some point the flux starts to deviate from the constant trend. That point marks the beginning of the shutdown regime, which corresponds to a convective coarsening of the flow structures, until diffusion predominates again. The processes of the individual stages will be explained in further detail later in this chapter.

Looking at the concentration field should additionally help with that description. That is why in Fig. 3.4 and 3.5 the concentration field in the vicinity of the top boundary is visualized over viscous time in the lower part of the figures in a so-called space-time plot. This shows in more detail the development of the plume roots. For better visibility, only a part of the domain width is shown. To see the different behaviors of the concentration in the different suggested regimes, the dissolution flux is displayed in the upper part of the figure and the times when the regime changes are indicated by dashed vertical lines. There is a change of behavior throughout the different stages visible in the change of the concentration distribution. The brighter and closer to white the color, the higher is the concentration, showing well the individual high concentration finger roots. This further encourages the suggested classification in the three main domains, diffusive, constant flux and shutdown.

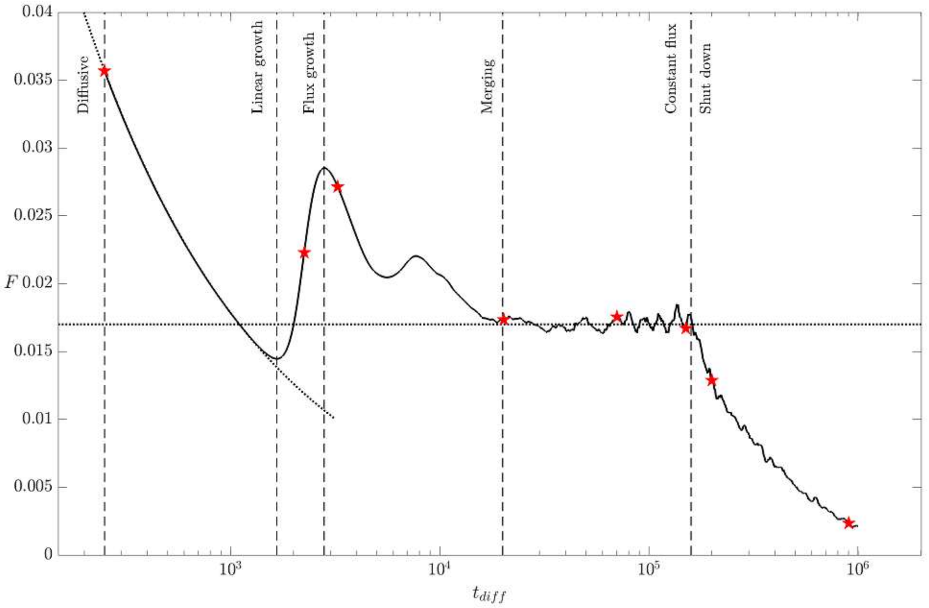

Figure 3.3 – Time behavior of the solute dissolution $F(t)$ for $Ra = 1 \times 10^4$. The dotted lines show the theoretical predictions for diffusive (Eq. 3.6) and constant flux regime (Eq. 3.7). The red stars are indicating the times at which the flow fields are visualized in Fig. 3.1. The dashed vertical lines indicate the different flow regimes.

### 3.2.1 Diffusion-dominated regime

The diffusive stage can be further divided into two subregimes. As long as convection is negligible, $F(t)$ can be modelled by the flux in a one-dimensional diffusion problem in a semi-infinite domain [8] by

$$F(t) = \frac{1}{\sqrt{\pi t}} \quad . \tag{3.6}$$

This model is valid for the first two regimes of solute transport: pure diffusion and linear growth. In these regimes, the dense fluid mixture of brine and $CO_2$ starts to accumulate and build a diffusive boundary layer at the top of the domain. The thicker this layer gets, the more unstable it becomes, resulting in the occurrence of first weak perturbations. They just decay at first though, due to the smoothing effect diffusion has and $F(t)$ keeps following the explained fit. Over time enough dense fluid accumulates over the lighter brine to make the perturbations stronger so they start to form convective fingers. These fingers are still rather undetectable in flow field visualizations (as seen in Fig. 3.1) but can be faintly seen in the space-time plot in Fig. 3.4 during the linear

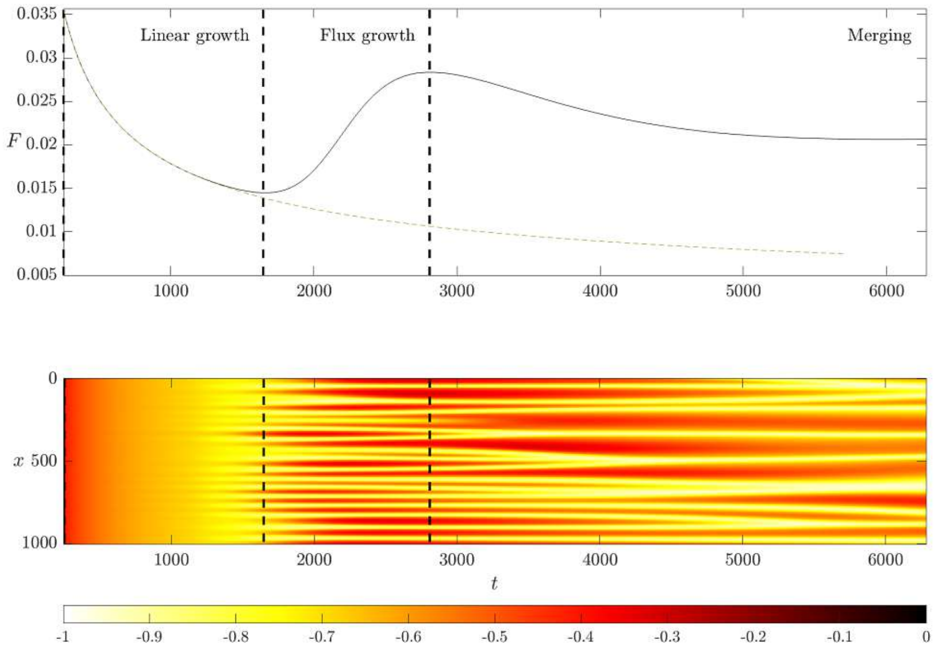

Figure 3.4 – Space-time diagram of the concentration field at a fixed height near the top of the domain for the first regimes of the process: diffusive, linear growth, flux growth and merging. To make the connection to the dissolution flux $F$, the latter is plotted in the top, with indication of the regimes by the dashed vertical lines.

growth stage. Well discernible is also the change of concentration in the boundary layer before the fingers form, making the layer denser and denser (color changing from red to orange) further contributing to it becoming unstable. At this point, mass transfer from the border into the boundary layer is dominated by diffusion.

### 3.2.2 Convection-dominated regime

As the name of the next regime, the flux growth regime, already suggests, during that stage the flux starts to increase. The beginning of this stage marks the departure of the flux curve from the purely diffusive model and so the entrance into the convection-dominated regime that entails four subregimes, the already mentioned constant flux regime being the most important one of them. The deviation of the flux from the diffusive model is explained by fingers becoming macroscopic and starting to accelerate downwards. In Fig. 3.4 it can be seen that they stay rather straight, not deviating to the sides. This is due to the high velocities of the fingers. Furthermore discernible there is that finger roots do not change during the transition to the flux growth stage. The formation of the fingers signifies the transport of fluid from the interface between boundary layer and empty domain and therefore a raise of the concentration gradient, as was already seen in Fig. 3.1. Corresponding to the rise of the flux, velocities and density inside the formed fingers get higher until individual fingers are large enough so they start to influence the velocity field in their vicinity, lowering velocities (visible in Fig. 3.1 from panel two to panel three in the right column). That corresponds to the time when the flux curve reaches a local maximum and the so-called merging stage commences, during which $F$ decreases. The effect the fingers have on each other is clearly visible in the space-time diagram: in the flux growth regime developed fingers start to merge together, resulting in a fewer number of overall plumes at the right of Fig. 3.4. In particular, fingers of the same size and length move towards each other and end up as one plume, while smaller fingers get pushed back by the upward return flow. These driven back fingers move to the sides as soon as they hit the top boundary, thus bolstering the movement of the bigger fingers towards each other [48]. An important detail visible in the space-time plot is the fact that the merging of the fingers happens from the root downwards. Due to that process, the number of fingers reduces while the space between the fingers increases. Also, the borders between fingers seem to soften with time, gradients are not as sharp anymore.

During the merging stage, the dissolution flux rises to another local maximum. This was explained by the thickening of the diffusive boundary layer as a result of this 'coarsening' process by Fu et al. [19]. A thicker diffusive layer in turn reduces the concentration gradient. As already introduced before, a higher concentration gradient results in an increase of the flux while on the contrary a lower one decreases the flux. During the rise of $F$ to that local maximum, the boundary layer thickens again, until it becomes too unstable once more and new so called "protoplumes" form [24, 25]. This explains the decline in the dissolution flux before hitting the constant behavior that declares the commencement of the next regime, the constant flux regime.

### Constant Flux Regime

During this stage, the dissolution flux oscillates around a constant value. This happens independently of the Rayleigh Darcy number and can be modelled in dimensionless form as

$$F(t) \approx 0.017 \tag{3.7}$$

as proposed by Hidalgo et al., Pau et al. and Slim [28, 40, 48] and confirmed by many others. As also shown by De Paoli et al. [11], independently of the initial condition, the constant flux regime is in very good agreement with the suggested model and thus also with past research results, as can be seen in Fig. 3.3. There, the prediction of Eq. 3.7 is shown as the horizontal dotted line. The starting time of this regime could be identified by determining the moment when $F$ starts fluctuating around the proposed value of 0.017. This is rather difficult in this case though, because fluctuations are generally high at the beginning of the constant flux regime. Slim [48] explains the difficulty in finding the exact time through the spatial heterogeneity of the timing for reaching this stage and furthermore says that it is dependent on the initial condition. She suggested a starting time between 16000 and 40000 in diffusive units. In the following, if not differently declared, the onset time of constant flux is $t = 2 \cdot 10^4$.

This regime is all about growth of already existing fingers. The newly formed, smaller protoplumes get pushed by the before described upward flow (background flow) towards the primary plumes. That mechanism results in the "fishbone pattern" [25] of the space-time diagram at later times in Fig. 3.5. Only the protoplumes make fingers larger at this point, while the merging of primary plumes as it happened in the regime before becomes sporadic. Instead, Slim [48] describes a new mechanism that she calls "slip-streaming". It is the merging of two plumes further down the domain as opposed to at the roots. The primary plumes are discernible in the flow visualizations of Fig. 3.1 as very long and thin, descending into the domain filled with fresh fluid. These mechanisms feed the fingers and push them further down into the domain.

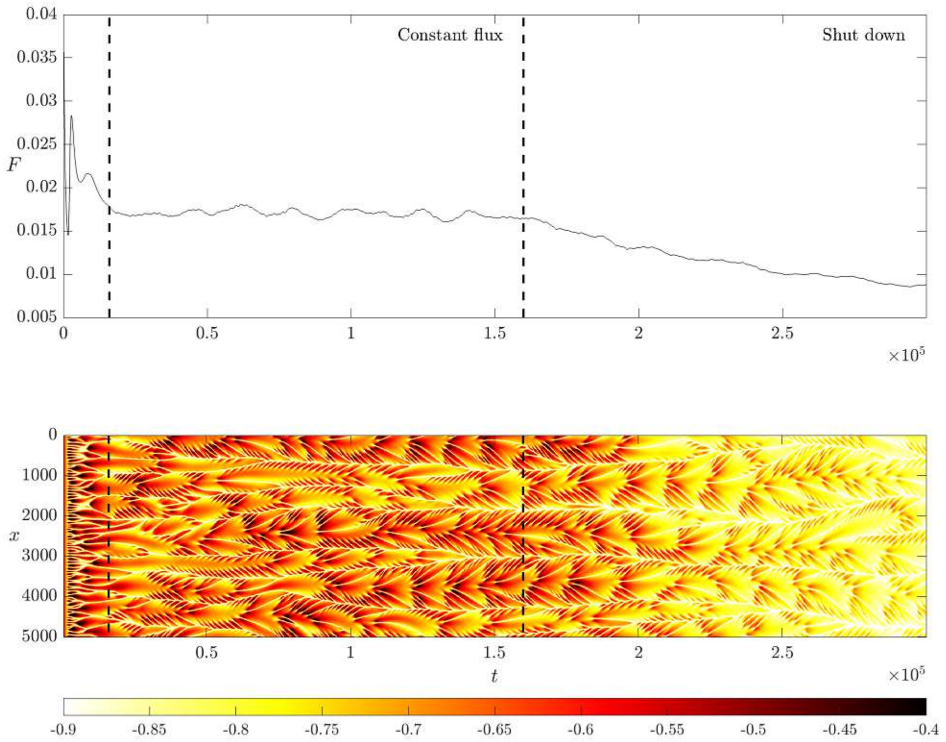

Figure 3.5 – Space-time diagram of the concentration field at a fixed height near the top of the domain for the whole simulation. Here the constant flux and the shutdown stage are better visible.

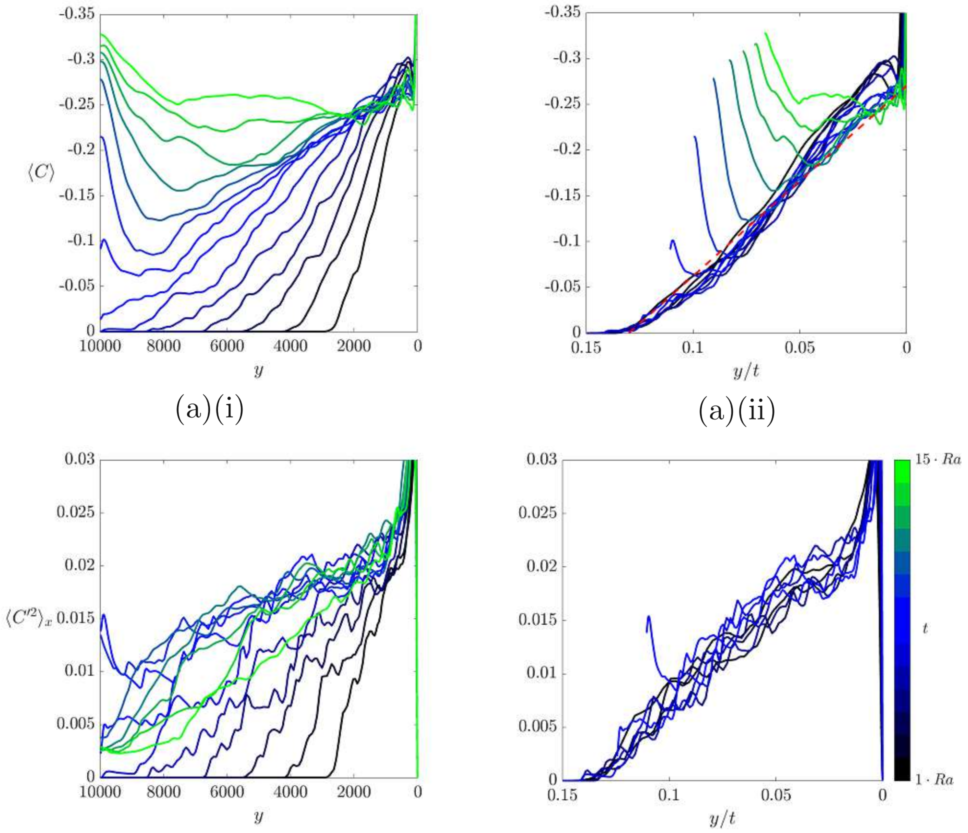

(a)(i) (a)(ii)

(b)(i) (b)(ii)

Figure 3.6 – Concentration profiles (a) and profiles of the concentration variance (b) plotted over the domain height for the reference simulation of $Ra = 1 \times 10^4$ at different times in the constant flux regime. In the right column, the profiles are plotted over the similarity variable $y/t$. The red dashed line is the self-similarity solution of Eq. 3.8.

Since the dissolution flux as well as the space-time plot have the described constant behavior, in Fig. 3.6(a) horizontally averaged concentration profiles and in (b) concentration variance profiles at different times in diffusive units are shown over the height of the domain. The black curves correspond to times at the beginning of the constant flux regime, the lighter in color they get the later the corresponding time.

First looking at the upper part (a) of the figure, where the concentration is shown, an almost linear trend of the concentration profiles ((a)(i)) is noticeable before the fingers reach the bottom boundary. The profiles change to a bi-linear behavior (more on that later) to smooth out and become almost straight as a precursor of the next regime. Plotting the profile in terms of the similarity variable $y/t$, the concentration profiles appear self-similar (see Fig. 3.6 (a)(ii)) Justification of this choice of similarity solution is given by Slim [48] due to the missing apparent length scale in both directions. The height of the domain $L_y$ is not relevant during the growth of the primary plumes and the width has already been shown to have no influence. This linear prediction of $\langle C\rangle_x$ when using the similarity variable was expressed by Slim [48] as

$$\langle C\rangle_x \approx C_1(t)\left[1+\frac{y}{wt}\right] \quad , \tag{3.8}$$

defining $C_1 = 0.27$ as the position when linear dependence is exhibited and $w = -0.13$ as the velocity of the plume tips. De Paoli et al. [11] showed a similar trend with slightly different values for the two constants, $-0.26 < C_1 < -0.21$ and $w = -0.16$. As discoverable in Fig. 3.6 (a)(i), $C_1$ ranges from $-0.25$ to $-0.3$ in this case. Plotted in Fig. 3.6 (a)(ii) as a dashed red line is Eq. 3.8 with the values proposed by Slim, with which the results show very good agreement.

At Fig. 3.6 (b), the variance of the concentration,

$$\langle C'^2\rangle_x = \langle C^2\rangle_x - \langle C\rangle_x^2 \tag{3.9}$$

is looked at. The biggest values for the fluctuations occur near the top boundary, then, at early times, they reduce until reaching zero at the point where fingers currently are. The unstable behavior of the curves remains until after fingers have reached the bottom. At later times (green in color) the curves become smoother and values return close to zero for the lower part of the domain. This corresponds to the reduction of the flow activity near the bottom where, as shown before, fingers become less and less distinct. These profiles can be plotted over the similarity variable, $y/t$ again. This is shown in (b)(ii) to show a self-similar trend in the first part of the constant flux regime. Profiles at later times do not follow that tendency and are thus not depicted.

The mentioned linear and bi-linear shape of the concentration profiles is getting further examined in Fig. 3.7. It shows two concentration profiles at different times over the domain height. The first time point is correspondent to the fingers reaching the bottom boundary, while the second one depicts a later time, still during constant flux though. The profiles follow the model

$$\langle C(y,t)\rangle_x = -\frac{C_1}{y_1(t)}[y - y_1(t)] \tag{3.10}$$

as suggested by De Paoli et al. [11]. Note that $y_1(t)$ is the position of the fingers at time $t$. Here, as just discussed above, $C_1$ is chosen as -0.27. For the time at which the fingers reach the bottom boundary, i.e. when $y_1(t = 7 \cdot Ra) = 0$, Eq. 3.10 becomes

$$\langle C(y, t = 7 \cdot Ra)\rangle_x = 0.27y \quad , \tag{3.11}$$

which is shown in Fig. 3.7 (a) as the dotted line. The results are closely following the model.

After contact of the plumes on the bottom boundary, the filling up of the domain with dense fluid is well visible in the bi-linear shape of the concentration profile as shown in Fig. 3.7 (b). The profile exhibits a knee which moves upwards with time, described by De Paoli et al. [11] as

$$y_2(t) = -w[t - (1+\eta)t_b] \quad , \tag{3.12}$$

with $\eta = 0.4$ and $t_b = 7 \cdot Ra$. The prediction is not followed by the results of this work but the bi-linearity of the concentration profiles is nonetheless well visible, indicated by the bold dotted lines. The faint dotted lines are depicting firstly $C_1$, which stays in the same range as before for profiles that follow the bi-linear behavior and secondly the current position of the knee $y_2$ calculated by Eq. 3.12. For this specific time step, it seems to depict the correct position. Tried for other time steps, the prediction does not fit as well though, resulting in larger values for $y_2$ than the bend is actually at. With time, the entire domain slowly gets saturated with dissolved fluid. The upward

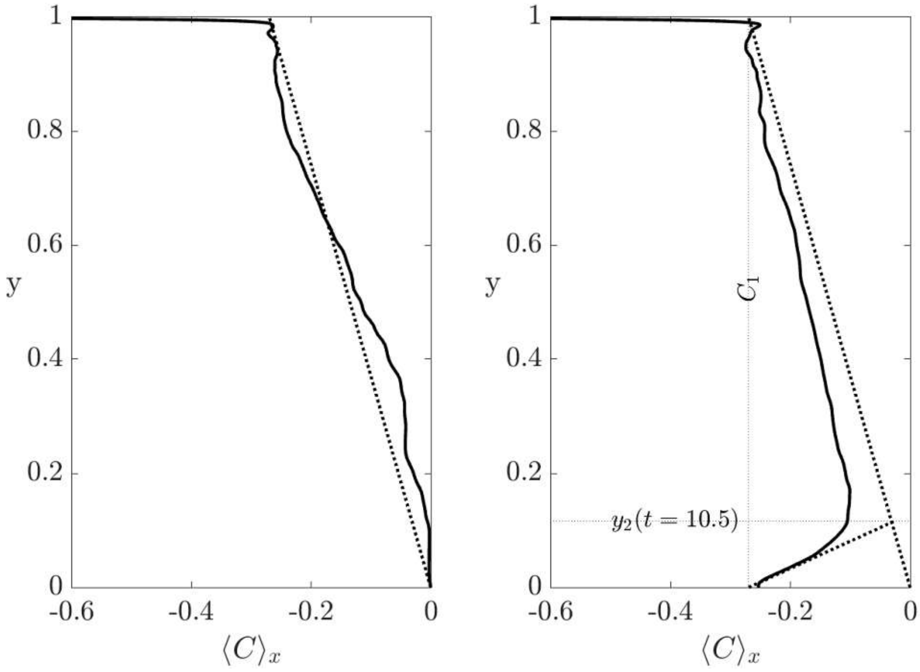

(a) (b)

Figure 3.7 – Concentration profiles in dependency of the domain height (y-axis) at times (a): $t = 7 \cdot Ra$ and (b): $t = 10.5 \cdot Ra$. The bold dashed lines show the models introduced by Eq. 3.10 and 3.11

movement of this knee is even better visible in the depiction of $\langle C \rangle$ over $y/t$ in Fig. 3.6. The bend in the concentration profile moves from the bottom of the domain all the way to the top (from left to right in the plot). The time corresponding to the wedge arriving at the top boundary is the time when the information about the end of the domain travelled back up. This marks the beginning of the next flow regime, the shutdown regime.

### 3.2.3 Shutdown Regime

Considering the behavior of the flux $F(t)$, a rapid change, which identifies the new regime, can be recognized as the deviation from the constant flux at 0.017. Flux values start to steadily decline. With this reduction of values, convection reduces as well, while diffusive mechanisms become stronger.

To describe the descending trend of $F$ in that regime of $t > 16 \cdot Ra$ two approaches

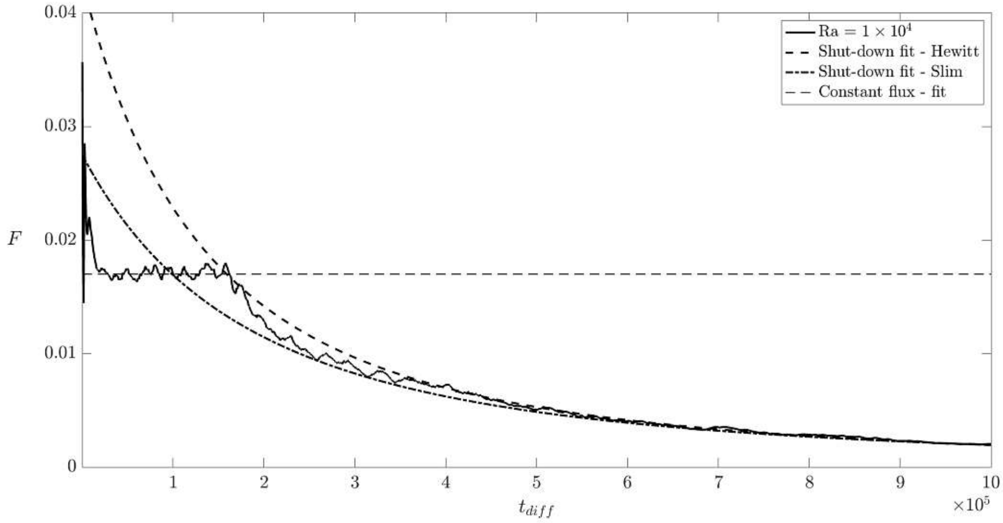

Figure 3.8 – Dissolution flux over diffusive time for the reference simulation at $Ra = 1 \times 10^4$ to compare it to the introduced models during the shutdown regime by Hewitt et al. [48] (dashed) and Slim [48] (dotdashed).

have been suggested. Firstly there is the one by Hewitt et al. [25]

$$F(t) = \frac{4 \cdot 0.00688}{1 + 4 \cdot 0.00688 \cdot t/Ra} \tag{3.13}$$

and secondly the one by Slim [48]

$$F(t) = \frac{16.8}{[0.73(t/Ra - 16) + 31.5]^2} \quad . \tag{3.14}$$

Fig. 3.8 shows the dissolution flux, $F(t)$ over time in diffusive units, at late times. Also plotted are the just introduced models, dashed Eq. 3.13 (Hewitt et al. [25]) and dotdashed Eq. 3.14 (Slim [48]). Eq. 3.13 seems to follow the results very well. The actual curve in the shutdown regime lies in between the two models. For later times, there is a very good agreement with both models.

As visible in the space-time plot in Fig. 3.5 the root behavior of the fingers does not change significantly with transition to the last regime. Mergers and initiation of new fingers from the boundary layer just become rarer with further saturation of the domain. Looking at the horizontally averaged concentration profiles in Fig. 3.9 (a), now for the later times of shutdown, it can be seen that the fluids are already well mixed by this point, showing an almost linear profile over the height. With time (from black curves to green) the value at which the profiles are, moves towards −1 which is the concentration

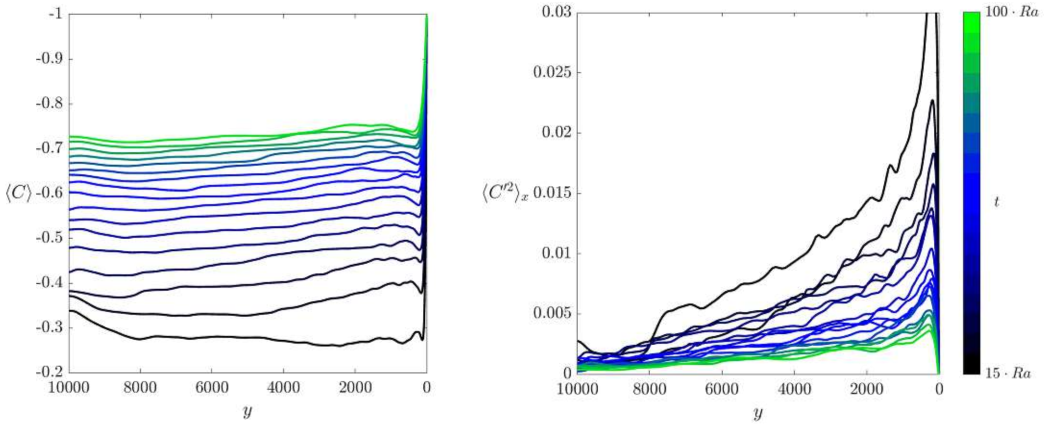

(a) (b)

Figure 3.9 – Concentration profiles (a) and profiles of the concentration variance plotted (b) over the domain height for the reference simulation at different times in the shutdown regime.

of $CO_2$ that the whole domain ultimately will have. This can also be shown by plotting the average interior concentration over time in convective units, as done in Fig. 3.10 (a). Note that $\theta(t)$ is defined as

$$\theta(t) = \int_0^W \int_0^1 C(x, y, t) dx dy \tag{3.15}$$

by Hewitt et al. [25] and exhibits a strong increase in the first part of the simulations to later asymptotically approach $-1$.

Fluctuations of the concentration shown on the right of Fig. 3.9 are still highest near the top boundary but become smaller and smaller over the whole domain with the progression of time. This indicates the takeover of diffusive effects, reducing velocities and fluctuations in the flow by extending flow structures. This coarsening was already shown before, in the size of flow structures in Fig. 3.2. To describe this enlargement of the flow structures in more detail, the time-behavior of the average wavenumber can be looked at, at late times. In Fig. 3.10 (b) $\langle k \rangle_x$ (defined in Eq. 3.4) over the effective Rayleigh Darcy number $Ra_e$ is plotted. Note that $Ra_e$ is defined as

$$Ra_e = 4Ra_0 \mid \theta(t) \mid \tag{3.16}$$

by Hewitt et al. [25] and was introduced to facilitate the comparison with a different configuration [10, 25]. Excellent agreement with previous results (Hewitt et al. [25]) is

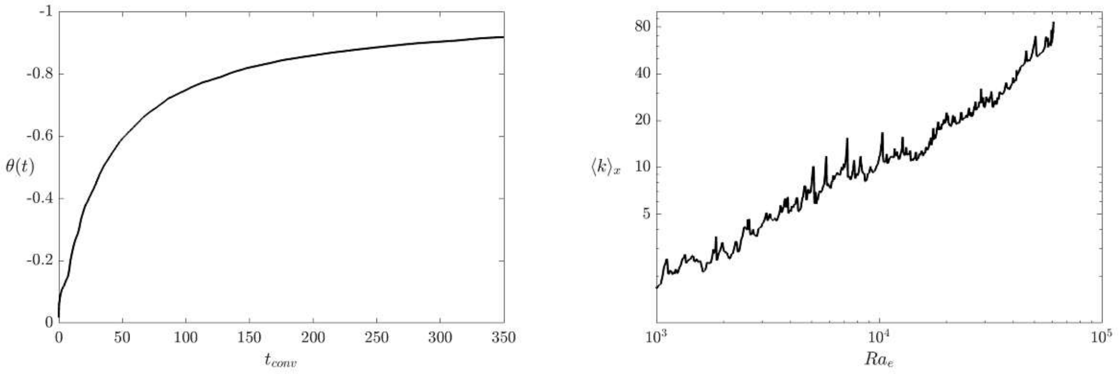

(a) (b)

Figure 3.10 – Shutdown behavior of wavenumber $\langle k \rangle_x$ for $Ra = 2 \times 10^4$: (a) average interior concentration $\theta(t)$ plotted over time and (b) average wavenumber $\langle k \rangle_x$ measured at $y = 0.5$ and plotted against the effective Rayleigh Darcy number $Ra_e$ for times $> 15 \cdot Ra$

obtained.

## 3.3 Measures of Mixing

As already mentioned, to characterize fluid transport, the dissolution flux $F$ can easily be used. There are however further measures that focus on the amount of mixing, which can give even more insights into the flow dynamics. These measures will be explored in the next chapters.

### 3.3.1 Mean scalar dissipation rate $\langle \chi \rangle$

Firstly, there is the mean scalar dissipation rate $\langle \chi \rangle$ [5, 28, 39]. It is originally defined from the local concentration gradients [44], and adapted to the case of solutal convection in porous media [28] as

$$\langle \chi \rangle_{x,y} = \langle \nabla C \cdot Ra^{-1} \nabla C \rangle_{x,y} \quad . \tag{3.17}$$

This quantity measures the mean mixing rate, since mixing gets stronger with higher concentration gradients [5]. Note that $\langle \cdot \rangle_{x,y}$ here, as opposed to $\langle \cdot \rangle_x$ which was used in the chapter before, is the mean in both spatial directions and therefore the surface integral $\langle a \rangle_{x,y}(t) = \frac{1}{W} \int_0^W \int_0^1 a(x, y, t) dx dy$.

In Fig. 3.11 the time behavior of $\langle \chi \rangle_{x,y}$ is shown as the red curve plotted over time in diffusive units. It follows the same general trend of the dissolution flux where, after

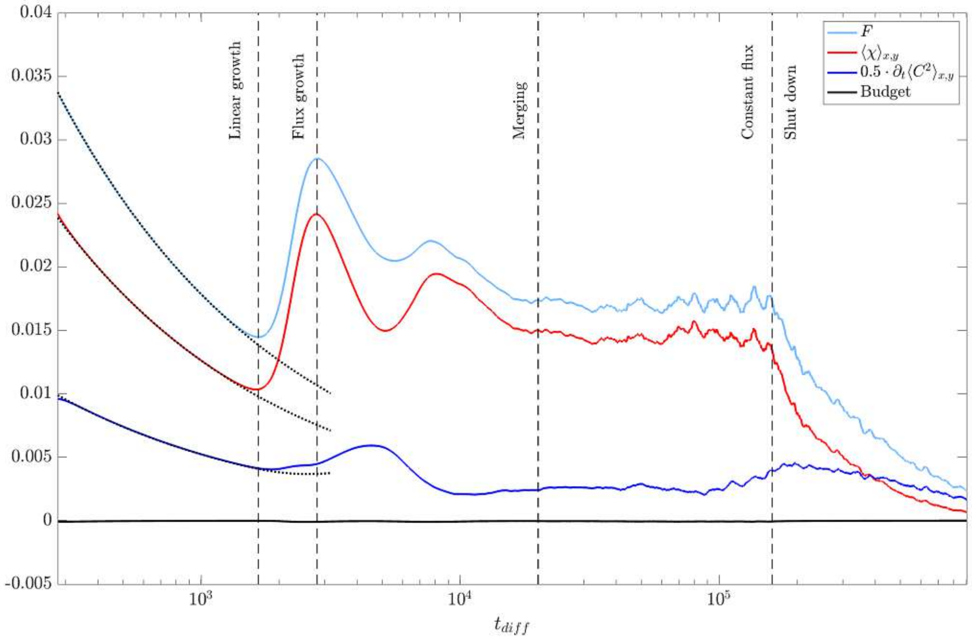

Figure 3.11 – Time behavior of dissolution flux $F$, mean scalar dissipation $\langle\chi\rangle_{x,y}$ and mixing rate for the reference simulation. of the budget (equation 3.21) is displayed in black and is zero throughout the whole simulation. Annotated with dotted lines are the fits for all three measures in the diffusive regime in the beginning of the simulations.

the initial decrease in the diffusive regime, the curve increases (meaning an increase in mixing during elevated finger growth in the linear growth regime starting from $t \approx 1.6 \cdot 10^3$). During the diffusive stage it follows the behavior

$$\langle\chi\rangle_{x,y} = \frac{1}{\sqrt{2\pi t}} \tag{3.18}$$

which is plotted as a dotted line in the figure. The following dip, explained by reintensified diffusion processes and merging of fingers in the merging regime, decreases the amount of mixing. During the constant flux regime, mixing stays constant as well, and then decreases at $t \approx 15 - 16 \cdot Ra$. This decrease is due to the progressive saturation of the layer, which means a constant concentration distribution and thus a lower and lower magnitude of mixing until a homogeneous solution is attained. The described behavior is in good agreement with the results of the concentration variance profiles as already shown in Fig. 3.9.

### 3.3.2 Mixing Rate $\frac{\partial\langle C^2\rangle}{\partial t}$

The mixing rate is defined as the change of the mean square concentration with time, and measures the variability of the spatial distribution of the concentration. In Fig. 3.11 the mixing rate is indicated by the blue line. The fitting of the curve to the model, proposed by Slim [48],

$$\frac{\partial\langle C^2\rangle_{x,y}}{\partial t} \approx \frac{1}{\sqrt{\pi t}} \cdot \left[2 + \sqrt{2}\,\mathrm{erf}\left(\frac{-Ra}{\sqrt{2t}}\right)\right] \quad , \tag{3.19}$$

is plotted as well. The almost perfect agreement of the computational results with the models, is a further indication of the quality of the results.

**Budget** The mean scalar dissipation rate, the mixing rate and the dissolution flux can be used to assess the accuracy of the computation [5]. The solute transport equation (advection diffusion) integrated over the domain and normalized over the horizontal direction [26, 28] results in

$$\frac{\partial\langle C^2\rangle_{x,y}}{\partial t} = 2(C_{top}F_{top} - \langle\chi\rangle_{x,y}) \quad , \tag{3.20}$$

which draws a link between dissolution flux $F_{top}$ at the top of the domain, mean scalar dissipation rate $\langle\chi\rangle$ and mixing rate $\frac{\partial\langle C^2\rangle}{\partial t}$. With $C_{top} = -1$ as the concentration at the top boundary, it becomes

$$\frac{\partial\langle C^2\rangle_{x,y}}{\partial t} = -2(F + \langle\chi\rangle_{x,y}) \quad ; \tag{3.21}$$

which, for the computation to be correct, has to be satisfied at all times. This is well shown by the black line labelled “Budget” in Fig. 3.11.

### 3.3.3 Mean wavenumber

The already introduced mean wavenumber can also give insight into the mixing dynamics [12]. Looking at the development of $\langle k_{top}\rangle_x$ of the top slice with time in Fig. 3.12, it is apparent that a behavior similar to the one of the flux is followed. With the start of convection, the decline of $\langle k_{top}\rangle_x$ is explained since the flow structures get bigger with the formation of the fingers. After that, fingers stay in the same order of magnitude as already shown in Fig. 3.2. This constant behavior lasts for as long as the constant flux regime continues. With the beginning of the shutdown regime, characteristic widths slowly enlarge in a similar way as the dissolution flux. This was also already established in Fig. 3.10.

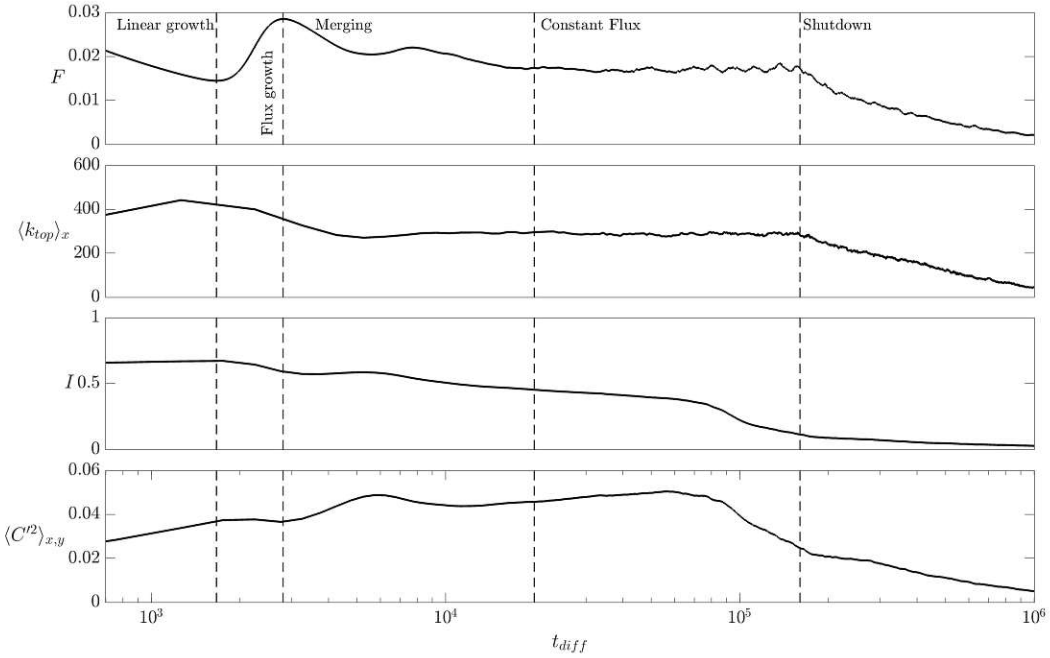

Figure 3.12 – Time behavior of mixing for the reference simulation at $Ra = 1 \times 10^4$. The vertical dashed lines mark the different regimes. Shown is the average wavenumber $\langle k_{top}\rangle_x$ at the top boundary, the intensity of segregation $I$ and the decay of the concentration variance $\langle C^2\rangle_{x,y}$ (as well as the dissolution flux $F$).

### 3.3.4 Intensity of Segregation

Using the approach of Borgne et al. [5], later adapted by Eckel and Pini [15], the degree of concentration homogeneity

$$I(t) = \frac{\langle C(x,y,t)^2\rangle_{x,y} - \langle C(x,y,t)\rangle_{x,y}^2}{\langle C(x,y,t)\rangle_{x,y}(C_{max} - \langle C(x,y,t)\rangle_{x,y})} \tag{3.22}$$

can be quantified. Note that $\langle\cdot\rangle_{x,y}$ represents the averaging in both spatial directions x and y. A value of $I = 0$ corresponds to complete mixing, whereas $I = 1$ corresponds to complete separation. The different regimes are again well discernible by the behavior of $I$. During diffusion, at the beginning of the process, $I$ is constant and has a relatively high value. This behavior can be easily explained, since mixing happens only in the diffusive boundary layer near the top boundary, while the rest of the domain is almost unaffected by solute transport. After diffusion, there is a steady decline of the segregation intensity with varying slopes. What is interesting to point out is the varying $I$ during the constant flux regime. At $t \approx 7 - 8 \cdot Ra$ there is a jump in the slope to a stronger decline. The jump correlates with the time at which the fingers reach the bottom boundary, and the following mixing increase due to the gradual dampening of local concentration gradients. The sharp decrease of $I$ just before the beginning of the shutdown regime is followed by a milder decrease to zero during the shutdown stage.

### 3.3.5 Concentration Variance

The concentration variance is defined by Hidalgo et al. [28] as

$$\langle C'^2 \rangle = \langle C^2 \rangle - \langle C \rangle^2 \quad . \tag{3.23}$$

The time behavior of the concentration variance, spatially averaged over both directions $\langle C'^2 \rangle_{x,y}$, is shown in Fig. 3.12 in the bottom panel. Differently from the intensity of segregation, it shows an increase during the first regimes. Even in this curve, the arrival of fingers at the bottom marks a changing point in the curve. From that point on, the slope changes to a sinking behavior which again gradually approaches zero, showing the dampening in the concentration gradients during shutdown.

## 3.4 Influence of Rayleigh Darcy number

This section is dedicated to the influence of the Rayleigh Darcy number on the behavior of the main flow quantities introduced before. All measures that follow the same trend of the flux, like mean wavenumber and mean scalar dissipation rate, are influenced similarly by changes in $Ra$. Similarity is most apparent in the flux, therefore we first look at $F$ in an exemplary way.

### 3.4.1 Dissolution Flux

As mentioned in Chapter 2, we performed simulations at $100 \leq Ra \leq 6 \times 10^4$. In Fig. 3.13 it is clear that the flux shows the same behavior for different Rayleigh numbers;

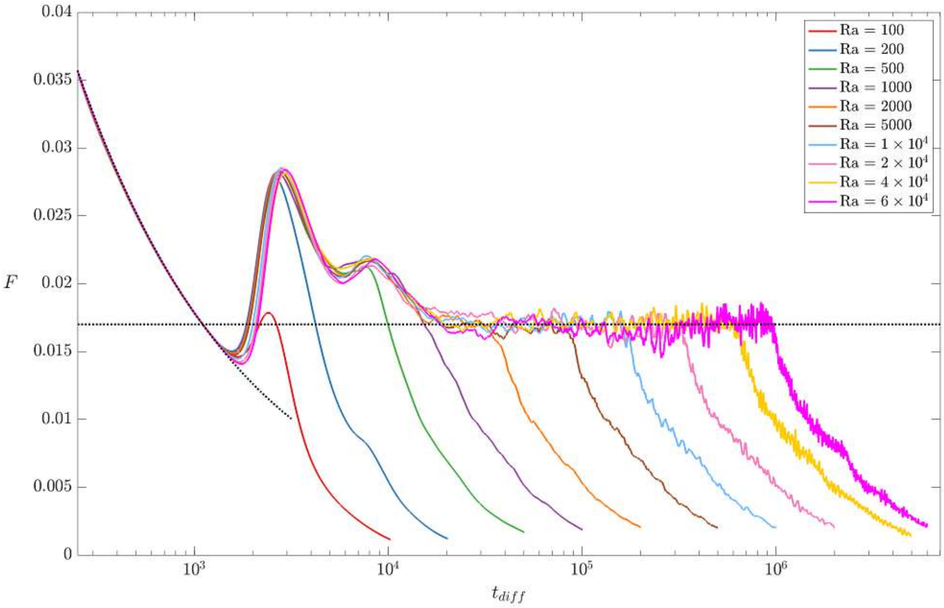

Figure 3.13 – Time behavior of the dimensionless dissolution flux $F(t)$ for all the performed simulations from $Ra = 100$ to $6 \times 10^4$.

the observed trend confirms previous results, like the ones achieved by Slim [48].

In the diffusive regime, $F(t)$ displays the very same behavior, no matter $Ra$. The small differences that are visible in the curves in Fig. 3.13 are due to the slightly different initial conditions, which result in slightly different onset times of convection. Simulations at lower Rayleigh Darcy numbers start deviating from the universal curve at some point. Convection for these cases stops earlier, and no constant flux regime is reached. To determine the Rayleigh Darcy numbers that undergo further flow development, one can just look at the quantitative trend of the dissolution flux. If the corresponding simulation reaches the behavior of fluctuations around the constant value of 0.017 then the existence of a constant flux regime can be assumed. A different, more precise way is to evaluate the amount of dissolved fluid $G(t)$. The amount of dissolved fluid from time $t_0$ to $t^*$ is defined as

$$G(t^*) = \int_{t_0}^{t^*} F(\tau^*) d\tau^* \quad . \tag{3.24}$$

The outcome for the reference simulation is shown in Fig. 3.14 (a) and is in very good agreement with the results of De Paoli et al. [11]. At the beginning of the simulation and especially in the constant flux regime, $G$ shows a strong increase, later it levels off, which corresponds to the weakening of convection in the shutdown regime. From

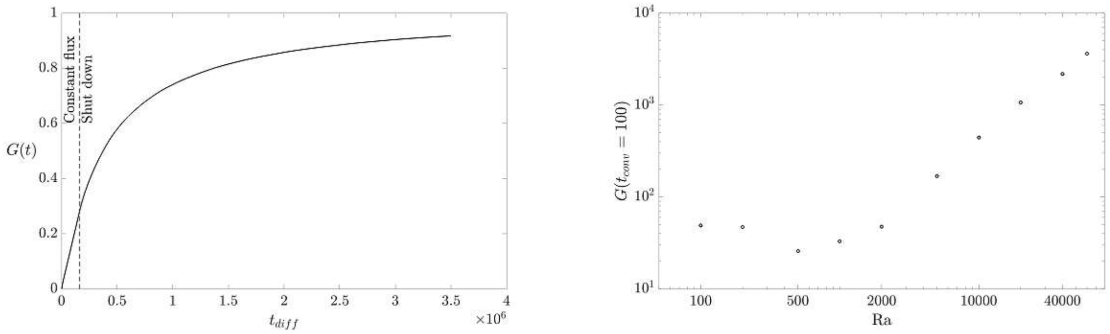

(a)

(b)

Figure 3.14 – Time behavior of dissolved fluid for the reference simulation and amount of dissolved fluid for different Rayleigh Darcy numbers at $t_{\text{conv}} = 100$

this behavior, it can be derived that most of the solute is dissolved during constant flux and shutdown regime. In (b) of Fig. 3.14 the amount of dissolved fluid at the end of the simulation at $t = 100 \cdot Ra$ is compared for different $Ra$. Due to its definition, the Rayleigh Darcy number has a strong influence on the amount of solute that can be dissolved in an aquifer. Simulations at lower $Ra$ dissolve approximately the same amount of fluid, while the simulations at higher $Ra$ show an increase in the total amount of dissolved fluid. This could be traced back to the missing constant flux stage in the behavior of $F$. The dependency of dissolved fluid on $Ra$ can be expressed as $G(t = 100) \sim Ra$. Based on these findings, the first Rayleigh Darcy number to be considered to have a distinct constant flux stage is chosen as $Ra = 5000$. Simulations with a Rayleigh Darcy number high enough to exhibit the constant flux stage also follow with a distinct shutdown regime. In the further extent of this work some measures that are inherent of the constant flux and shutdown regime are discussed and therefore only the simulations at $Ra > 5000$ are considered. First, an attempt to determine the onset time of the shutdown regime is made.

**Shutdown onset time** While the onset time of the constant flux regime is similar for all Rayleigh Darcy numbers, the time at which the fingers reach certain heights of the domain and therefore also the beginning of shutdown is very much dependent on $Ra$. This is also well visible in Fig. 3.13, where the time when the flux changes from the constant behavior is different for each simulation. To obtain the onset time of the convective shutdown, the derivative $\partial F/\partial t$ can be considered. More precisely, the time change in the derivative from zero shows the change in flux regime, as this is the time

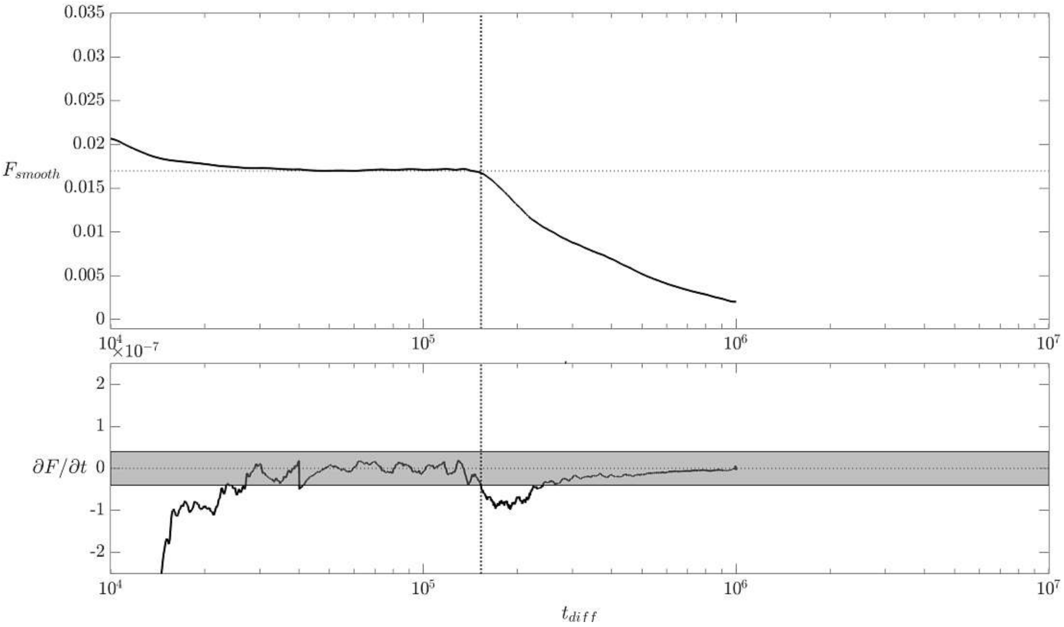

Figure 3.15 – Exemplary procedure to determine the onset time of shutdown, shown for $Ra = 1{\times}10^4$. In the upper part, the smoothed flux is shown for part of constant flux and shutdown regime and in the bottom figure the derivative of the flux $\partial F/\partial t$ is shown. The time when the derivative changes from zero is marked with a dotted line and is considered as the onset time for the shutdown regime.

when the flux starts decaying from the constant trend ($\partial F/\partial t \approx 0$). To find this point, first a smoothing operation was performed on the raw data of the flux $F$ in the region of interest ($2 \cdot 10^4 < t < 100 \cdot Ra$). The smoothed behavior is shown in Fig. 3.15 in the upper plot of the figure. The derivative of that smoothed curve was then calculated, shown in the lower part of the figure. Since the derivative is fluctuating around zero, the exact time at which it starts changing from zero was determined by calculating the standard deviation of the curve during the constant flux stage at $2 \cdot 10^4 < t < 15 \cdot Ra$. An area of twice the value of the standard deviation then was defined, as shown by the gray sector. As soon as the derivative deviates outside the indicated area, shutdown starts. That point is indicated by a vertical dotted line.

The described procedure was applied to all the other higher $Ra$ simulations, only adjusting the window size for the smoothing operation, making it larger for larger $Ra$. The decision to exclude $Ra = 2000$ from the Rayleigh Darcy numbers high enough to exhibit a constant flux regime is backed up by this computation of $\partial F/\partial t$. No part of the derivative shows a prolonged time where it has a value of zero, which means that the flux never reaches a constant value. To get more insights in the flow, the times

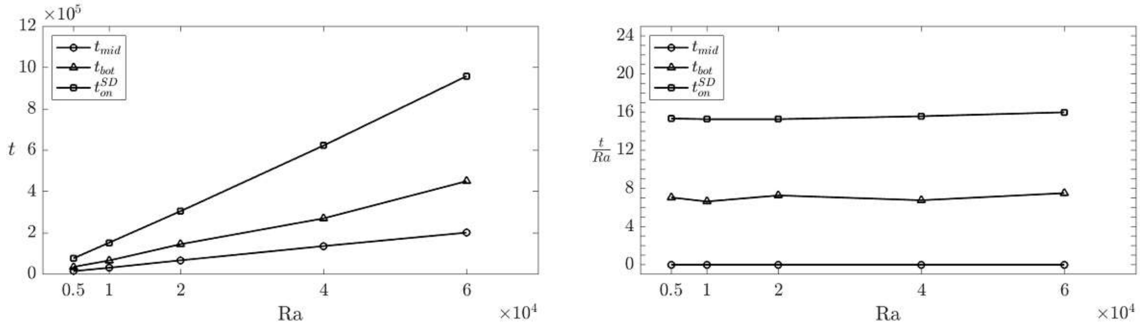

(a) (b)

Figure 3.16 – Times taken by the fingers to reach the middle and then the bottom of the domain, and finally the onset times of the shutdown regime, plotted against Rayleigh Darcy number in (a). (b) shows the same, but using the self-similar time $t/Ra$. In convective units $t_{bot} \approx 7$ and $t_{on}^{SD} = 15 - 16$.

when the fingers reach the middle and bottom of the domain were also computed using the behavior of the mean wavenumber over time. At heights not in the proximity of the top boundary, these trends exhibit a sharp peak at the point in time when the fingers reach the respective height.

While comparing the shutdown onset times in Fig. 3.16 (a), a linear dependence on $Ra$ becomes apparent. The times when the fingers reach certain heights of the domain show the very same behavior. The slope of the linear progress is not the same for these different points in time though.

Considering the self-similar time $t/Ra$ shown in Fig. 3.15 (b), the universal value for the start of the shutdown stage lies between $t_{on}^{SD} \approx 15 - 16$ which is in agreement with past research [48]. The time when plumes impact the bottom boundary results in $t_{bot} \approx 7$ which is however slightly different from Slim's [48] suggestion of $t_{bot} \approx 8$.

### 3.4.2 Characteristic length scale of flow structures

Not only the late behavior of the dissolution flux changes with changing Rayleigh Darcy number, but also the size of the flow structures is different. In Fig. 3.17 these differences are shown. They are rather visible comparing the values of the mean wavenumber averaged during the constant flux regime $\langle\lambda\rangle_t$, as done in the plot on the left side of the figure. But the characteristic size is also visible when looking at the actual finger sizes in the flow field visualization in the right part of the figure. Fingers for the same dimensionless domain size are bigger for $Ra = 5000$ (lower panel) than they are for

$Ra = 2 \times 10^4$ (upper panel). While looking at the flow field visualization, note that the plotted $\langle \lambda \rangle_t$ is measured near the top of the domain. Also note, that the value of $\lambda$ does not correspond to the spacing between plumes, but actually to the width of a single plume [48].

Compared to previous results (Fu et al. [19] and De Paoli et al. [10]), the results for $\langle \lambda \rangle_t$ are indeed in the same order of magnitude, although they are a bit lower here. The calculations are nonetheless consistent, since the power-law dependency $\lambda \sim Ra^{-1}$ described by Fu et al. [19] is observed. The explanation for the slightly different values might lie in the different evaluation method. Instead of using the Fourier transform like it was done in this work, previous works used an algorithm to count the number of peaks of a binarised concentration field. From that number, which corresponds to the amount of plumes, $\lambda$ can be derived.

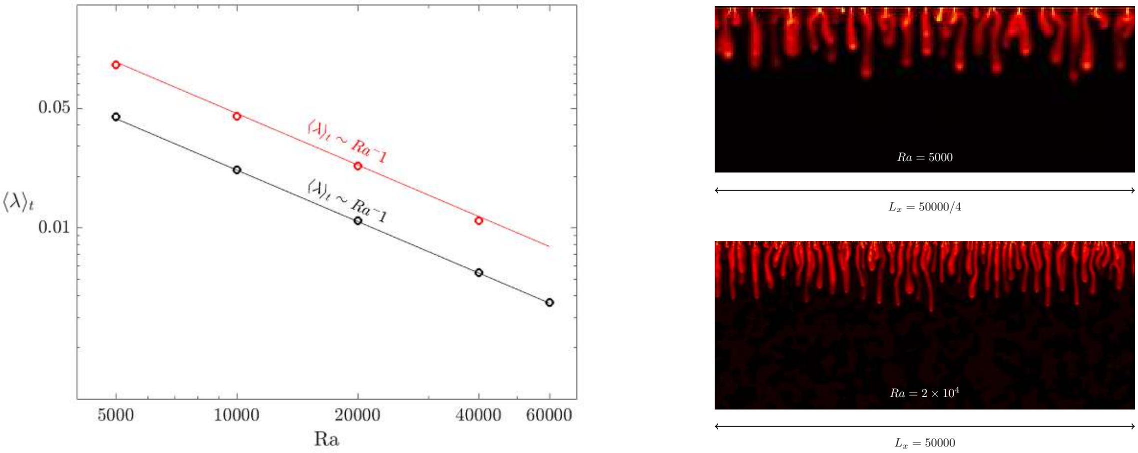

Figure 3.17 – Characteristic length scale $\langle \lambda \rangle_t$ of flow structures aka plume width in the vicinity of the top boundary in the constant flux regime for times $10 \cdot Ra < t < 15 \cdot Ra$ plotted against Rayleigh Darcy number. The dependency of $\lambda$ on $Ra$ is shown as the black curve connecting the points. The red dots are the results of Fu et al. [19] to compare. The right part shows the flow field visualizations for the simulations $Ra = 5 \times 10^3$ at the bottom and $Ra = 2 \times 10^4$ at the top. For better comparison, the domain size is constant in diffusive units.

# 4

# Conclusion

In this work we studied the problem of convective flow in fluid-saturated porous media, performing numerical investigations of the so-called one-sided configuration which is customarily used to reproduce the dissolution of liquid supercritical carbon dioxide into brine-filled aquifers deep underground. In chapter 2, the modelling of the problem was introduced, to also discuss further assessments and adjustments to the conducted numerical simulations. Results of these simulations were discussed in chapter 3. First, the time-dependent flow development was considered. In this case of convective dissolution, the flow forms vertical structures, called fingers or plumes. The development of these are observable in the visualization of the flow field and also when regarding the concentration profiles. Noticeable is the change in behavior and size of these fingers with time. Previous research studies introduced a classification into flow regimes [48]. Regarding the dissolution flux $F(t)$ near the top boundary proves as a straight-forward way to differentiate between the regimes. It follows a distinct behavior, regardless of the Rayleigh Darcy number. Regimes are a diffusion-dominated stage at the beginning, followed by the convection-dominated stage, entailing the constant flux regime and the so-called shutdown regime within which convection decays and diffusive effects take over once again. During the diffusive stage the dissolution flux exhibits a decline, the constant flux regime, shows fluctuations of $F(t)$ around a constant value of 0.017 and during the shutdown regime $F$ declines again, approaching zero at late times. The plume size can be quantified by the wavenumber $k$ from Fourier transforms performed on concentration distributions [43]. If a distribution at a certain height of the domain is chosen, the corresponding wavenumber at that specific location and time sheds light on the current width of the fingers. It was shown that not only the dissolution flux $F(t)$ but also dimensions and shapes of these flow structures change with advancing time, which is why further measures of mixing were introduced and their time behavior was discussed. Some of them like the mean scalar dissipation rate and the mean wavenumber show a very similar trend as the flux [12]. Others, like the concentration variance, but also the intensity of segregation do have a time dependency with the possibility of categorization into the introduced regimes but look qualitatively different from the flux curve. Simulations at different Rayleigh Darcy numbers ($100 \leq Ra \leq 6 \times 10^4$) were conducted to show the dependence of measures like flux and wavenumber on $Ra$. Comparisons were only conducted between relatively high Rayleigh Darcy numbers. A 'high enough' $Ra$ is reasoned by the existence of a distinctive constant flux regime when considering the time derivative of the dissolution flux and an increased value of dissolved solute $G(t)$. Simulations at higher Rayleigh Darcy numbers exhibit a longer constant flux regime. That is apparent in the dissolution flux trend but also by determining important time points of the simulation, e.g. the instance when the fingers first reach the bottom boundary, $t_{bot}$ or the end of the constant flux regime, $t_{on}^{SD}$. For these specific points in time a scaling of $t_{bot} = 7 - 8 \cdot Ra$ and $t_{on}^{SD} = 15 - 16 \cdot Ra$ could be introduced, showing a sole dependence on $Ra$. The larger amount of fluid that can get dissolved at higher $Ra$ is explainable by these longer process times. Regarding the finger sizes investigated by looking at the aforementioned wavenumber during the constant flux regime, an increase in $Ra$ means a decrease in structure sizes. A dependency of $\lambda \sim Ra^{-}1$ could be revealed.

For the highest possible safety in Carbon Dioxide Capture and Storage (CCS), where the aim is to separate $CO_2$ produced by big emitters from the flue gas and subsequently store it in aquifers deep underground, these just mentioned things are favorable [34]. First, a bigger amount of stored $CO_2$ is convenient for obvious reasons. Secondly, longer dissolution times mean longer safe storage since the carbon dioxide is flowing downwards further away from possible leaks or cracks that could release it back to the atmosphere. Aquifers with higher Rayleigh Darcy numbers are thus seemingly the best ones to choose for sequestration.

The results of this work are generally in very good agreement with already conducted research (among others [11, 12, 25, 48]), assessing the accuracy of the employed numerical tools. They can now be foreseen to further advance research in this area by expanding simulations to three dimensions first (already done by [14, 16, 19, 26]). Other ideas for subsequent simulations are to take properties of the aquifers like non-uniform permeability or porosity into account ([21]). Since timescales are so big, even the very slow background flow of groundwater in the reservoirs could also have an influence on dynamics and could be interesting to include in future research ([35]). It would also be interesting to look into a moving interface which better reproduces the change of the thickness of the layer of supercritical $CO_2$ with further dissolution into the depths of the reservoir ([25, 29]).

# Nomenclature

## Abbreviations

| | |
|---|---|
| AR | Aspect Ratio |
| CCS | Carbon Dioxide Capture and Sequestration |
| CFD | Computational Fluid Dynamics |
| CFL | Courant-Friedrichs-Lewy condition |
| $CO_2$ | Carbon Dioxide |
| DNS | Direct Numerical Simulation |
| EGR | Enhanced Gas Recovery |
| EOR | Enhanced Oil Recovery |
| RB | Rayleigh-Bénard |

## Symbols and Constants

| | |
|---|---|
| $\boldsymbol{u}$ | Volume averaged velocity field |
| $\chi$ | Scalar dissipation rate |
| $\Delta x$ | Grid resolution in x-direction |
| $\Delta y$ | Grid resolution in y-direction |
| $\kappa$ | Permeability |
| $\lambda$ | Inverse wavenumber or flow structure size indicator |
| $\mu$ | Viscosity |
| $\phi$ | Porosity |

| | |
|---|---|
| $\rho$ | Density |
| $\theta$ | Average interior concentration |
| $C$ | Concentration |
| $D$ | Diffusivity |
| $dt$ | Timesteps |
| $F$ | Dissolution flux |
| $G$ | Amount of dissolved fluid |
| $g$ | Gravity Acceleration |
| $H$ | Domain height |
| $I$ | Intensity of segregation |
| $k$ | Wavenumber |
| $L_x$ | Extension of the domain in x-direction |
| $L_y$ | Extension of the domain in y-direction |
| $N_x$ | Number of gridpoints in x-direction |
| $N_y$ | Number of gridpoints in y-direction |
| $p$ | Pressure |
| $t$ | Time |
| $t_{diff}$ | Time in diffusive units |
| $W$ | Domain width |
| $w$ | Velocity of plume tips |
| $Ra$ | Rayleigh Darcy Number |

# List of Figures

1.1 Schematic of Carbon Dioxide Capture and Sequestration - CCS . . . . 6

2.1 Sketch of the modelled domain . . . . . . . . . . . . . . . . . . . . . . . 12

2.2 Different grid resolutions on different domain sizes. The upper part shows quadratic domains ($L_x = L_y = 1$) with (a) a grid with an equal number of points in both directions ($N_x = N_y$) to start the grid assessment. Secondly, (b) shows a grid with an unequal number of points ($N_x > N_y$). (c) shows the change in domain size to a larger width, here resulting in an aspect ratio of $AR = L_x/L_y = 5$ to investigate influences of the domain width. . . . . . . . . . . . . . . . . . . . . . . . . . . . . . 16

2.3 Effect of grid refinement in x-direction on (a) mean flux $\langle F\rangle_t$ and (b) mean wavenumber $\langle k\rangle_{x,t}$. The dashed line in the left plot is marking the expected value of $\langle F\rangle_t$. The red dot marks the for this work, chosen resolution of $N_x = 1024$. . . . . . . . . . . . . . . . . . . . . . . . . . 17

2.4 Effect of grid refinement in y-direction on (a) mean flux $\langle F\rangle_t$ and (b) mean wavenumber $\langle k\rangle_{x,t}$. The dashed line again shows the expected value of 0.017 and the red dot marks the chosen resolution of $N_y = 256$. 18

2.5 Effect of domain width on (a) mean flux $\langle F\rangle_t$ and (b) mean wavenumber $\langle k\rangle_{x,t}$. The aspect ratio used in this work - $AR = 5$ - is indicated by the red dot. . . . . . . . . . . . . . . . . . . . . . . . . . . . . . . . . . 20

2.6 Time behavior of the timesteps for the simulation $\mathrm{S}_{10000}$ at $Ra = 1 \times 10^4$ to compare an introduced timestep limitation with the behaviour when no limitation is applied. . . . . . . . . . . . . . . . . . . . . . . . . . . 22

3.1 Solute transport in a porous domain in 2D at aspect ratio $AR = 5$, at $Ra = 1 \times 10^4$. Left column: behavior of the solute concentration distribution shown on a quadratic section of the whole domain. Central column: average concentration profile, $\langle C \rangle_x$. Right column: velocity variance, $\langle v_y'^2 \rangle_x$. The plots in center and right are profiles averaged over the width of the domain and plotted over the height. Each row, from top to bottom, corresponds to a different, later time instant, as explicitly labelled. . . . . . . . . . . . . . . . . . . . . . . . . . . . . . . . 25

3.1 Solute transport in a porous domain in 2D at aspect ratio $AR = 5$, at $Ra = 1 \times 10^4$. Left column: behavior of the solute concentration distribution shown on a quadratic section of the domain. Central column: average concentration profile, $\langle C \rangle_x$. Right column: velocity variance, $\langle v_y'^2 \rangle_x$. The plots in center and right are profiles averaged over the width of the domain and plotted over the height. Each row, from top to bottom, corresponds to a different, later time instant, as explicitly labelled. . . . 26

3.2 The size of flow structures $\lambda$ at different heights of the domain at two points in time for the simulation at $Ra = 1 \times 10^4$. The heights are indicated as white dashed lines on the right visualization. . . . . . . . . 28

3.3 Time behavior of the solute dissolution $F(t)$ for $Ra = 1 \times 10^4$. The dotted lines show the theoretical predictions for diffusive (Eq. 3.6) and constant flux regime (Eq. 3.7). The red stars are indicating the times at which the flow fields are visualized in Fig. 3.1. The dashed vertical lines indicate the different flow regimes. . . . . . . . . . . . . . . . . . . . . . 30

3.4 Space-time diagram of the concentration field at a fixed height near the top of the domain for the first regimes of the process: diffusive, linear growth, flux growth and merging. To make the connection to the dissolution flux $F$, the latter is plotted in the top, with indication of the regimes by the dashed vertical lines. . . . . . . . . . . . . . . . . . . . . . 31

3.5 Space-time diagram of the concentration field at a fixed height near the top of the domain for the whole simulation. Here the constant flux and the shutdown stage are better visible. . . . . . . . . . . . . . . . . . . . . 34

3.6 Concentration profiles (a) and profiles of the concentration variance (b) plotted over the domain height for the reference simulation of $Ra = 1 \times 10^4$ at different times in the constant flux regime. In the right column, the profiles are plotted over the similarity variable $y/t$. The red dashed line is the self-similarity solution of Eq. 3.8. . . . . . . . . . . . . . . . . . . 34

3.7 Concentration profiles in dependency of the domain height (y-axis) at times (a): $t = 7 \cdot Ra$ and (b): $t = 10.5 \cdot Ra$. The bold dashed lines show the models introduced by Eq. 3.10 and 3.11 . . . . . . . . . . . . . . . 37

3.8 Dissolution flux over diffusive time for the reference simulation at $Ra = 1 \times 10^4$ to compare it to the introduced models during the shutdown regime by Hewitt et al. [48] (dashed) and Slim [48] (dotdashed). . . . . 38

3.9 Concentration profiles (a) and profiles of the concentration variance plotted (b) over the domain height for the reference simulation at different times in the shutdown regime. . . . . . . . . . . . . . . . . . . . . . 39

3.10 Shutdown behavior of wavenumber $\langle k \rangle_x$ for $Ra = 2 \times 10^4$: (a) average interior concentration $\theta(t)$ plotted over time and (b) average wavenumber $\langle k \rangle_x$ measured at $y = 0.5$ and plotted against the effective Rayleigh Darcy number $Ra_e$ for times $> 15 \cdot Ra$ . . . . . . . . . . . . . . . . . . 40

3.11 Time behavior of dissolution flux $F$, mean scalar dissipation $\langle \chi \rangle_{x,y}$ and mixing rate for the reference simulation. of the budget (equation 3.21) is displayed in black and is zero throughout the whole simulation. Annotated with dotted lines are the fits for all three measures in the diffusive regime in the beginning of the simulations. . . . . . . . . . . . . . . . 41

3.12 Time behavior of mixing for the reference simulation at $Ra = 1 \times 10^4$. The vertical dashed lines mark the different regimes. Shown is the average wavenumber $\langle k_{top} \rangle_x$ at the top boundary, the intensity of segregation $I$ and the decay of the concentration variance $\langle C^2 \rangle_{x,y}$ (as well as the dissolution flux $F$). . . . . . . . . . . . . . . . . . . . . . . . . . . 43

3.13 Time behavior of the dimensionless dissolution flux $F(t)$ for all the performed simulations from $Ra = 100$ to $6 \times 10^4$. . . . . . . . . . . . . 45

3.14 Time behavior of dissolved fluid for the reference simulation and amount of dissolved fluid for different Rayleigh Darcy numbers at $t_{\mathrm{conv}} = 100$ . 46

3.15 Exemplary procedure to determine the onset time of shutdown, shown for $Ra = 1 \times 10^4$. In the upper part, the smoothed flux is shown for part of constant flux and shutdown regime and in the bottom figure the derivative of the flux $\partial F/\partial t$ is shown. The time when the derivative changes from zero is marked with a dotted line and is considered as the onset time for the shutdown regime. . . . . . . . . . . . . . . . . . . . . 47

3.16 Times taken by the fingers to reach the middle and then the bottom of the domain, and finally the onset times of the shutdown regime, plotted against Rayleigh Darcy number in (a). (b) shows the same, but using the self-similar time $t/Ra$. In convective units $t_{bot} \approx 7$ and $t_{on}^{SD} = 15 - 16$. 48

3.17 Characteristic length scale $\langle\lambda\rangle_t$ of flow structures aka plume width in the vicinity of the top boundary in the constant flux regime for times $10 \cdot Ra < t < 15 \cdot Ra$ plotted against Rayleigh Darcy number. The dependency of $\lambda$ on $Ra$ is shown as the black curve connecting the points. The red dots are the results of Fu et al. [19] to compare. The right part shows the flow field visualizations for the simulations $Ra = 5 \times 10^3$ at the bottom and $Ra = 2 \times 10^4$ at the top. For better comparison, the domain size is constant in diffusive units. . . . . . . . . . . . . . . . . . 49

# List of Tables

2.1 Effect of the domain size (horizontal aspect ratio, $AR = L_x/L_y$) on the flow at $Ra = 1 \times 10^4$. Different aspect ratios in the range $0.5 \leq AR \leq 20.0$ are considered while keeping the resolution constant. Mean flux, averaged over the whole timespan ($\langle F \rangle_t$) and calculated with a running average ($\langle F \rangle_t^{MM}$, window size for the running average was taken as 1/4 of the recorded points during the looked at time span) as well as their fluctuations $\sigma$ are stated. . . . . . . . . . . . . . . . . . . . . . . . . . . . 19

2.2 Details of the simulation parameters for the performed simulations. In the last column the mean flux during the constant flux regime from $2 \cdot 10^4 < t < 15 \cdot Ra$ is displayed. . . . . . . . . . . . . . . . . . . . . . . . 20

# Bibliography

[1] Global monthly mean co2. https://gml.noaa.gov/ccgg/trends/monthly.html. Accessed: 2024-05-06.

[2] Stefan Bachu. Screening and ranking of sedimentary basins for sequestration of co2 in geological media in response to climate change. *Environmental Geology*, 44 (3):277–289, 2003.

[3] Stefan Bachu. Co2 storage in geological media: Role, means, status and barriers to deployment. *Progress in energy and combustion science*, 34(2):254–273, 2008.

[4] Stefan Bachu, WD Gunter, and EH Perkins. Aquifer disposal of co2: hydrodynamic and mineral trapping. *Energy Conversion and management*, 35(4):269–279, 1994.

[5] Tanguy Le Borgne, Marco Dentz, Diogo Bolster, Jesus Carrera, Jean Raynald de Dreuzy, and Philippe Davy. Non-fickian mixing: Temporal evolution of the scalar dissipation rate in heterogeneous porous media. *Advances in Water Resources*, 33: 1468–1475, 12 2010. ISSN 0309-1708. doi: 10.1016/J.ADVWATRES.2010.08.006.

[6] M. A. Celia, S. Bachu, J. M. Nordbotten, and K. W. Bandilla. Status of co2 storage in deep saline aquifers with emphasis on modeling approaches and practical simulations. *Water Resources Research*, 51:6846–6892, 9 2015. ISSN 1944-7973. doi: 10.1002/2015WR017609. URL https://onlinelibrary.wiley.com/doi/abs/10.1002/2015WR017609.

[7] Ilia Cherezov. Modelling convective dissolution and reaction of carbon dioxide in saline aquifers. 2017. doi: https://doi.org/10.17863/CAM.14371.

[8] John Crank. *The mathematics of diffusion*. Oxford university press, 1979.

[9] Marco De Paoli. Convective mixing in porous media: a review of darcy, pore-scale and hele-shaw studies. *The European Physical Journal E 2023 46:12*, 46:1–26,

12 2023. ISSN 1292-895X. doi: 10.1140/EPJE/S10189-023-00390-8. URL https://link.springer.com/article/10.1140/epje/s10189-023-00390-8.

[10] Marco De Paoli, Francesco Zonta, and Alfredo Soldati. Influence of anisotropic permeability on convection in porous media: Implications for geological co2 sequestration. *Physics of fluids*, 28(5), 2016.

[11] Marco De Paoli, Francesco Zonta, and Alfredo Soldati. Dissolution in anisotropic porous media: Modelling convection regimes from onset to shutdown. *Physics of Fluids*, 29:1–9, 2 2017. ISSN 10897666. doi: 10.1063/1.4975393.

[12] Marco De Paoli, Vlad Giurgiu, Francesco Zonta, and Alfredo Soldati. Universal behavior of scalar dissipation rate in confined porous media. *Physical Review Fluids*, 4:101501, 10 2019. ISSN 2469990X. doi: 10.1103/PHYSREVFLUIDS.4.101501/FIGURES/4/MEDIUM. URL https://journals.aps.org/prfluids/abstract/10.1103/PhysRevFluids.4.101501.

[13] Marco De Paoli, Francesco Zonta, and Alfredo Soldati. Rayleigh-taylor convective dissolution in confined porous media. *Physical Review Fluids*, 4:023502, 2 2019. ISSN 2469990X. doi: 10.1103/PHYSREVFLUIDS.4.023502/FIGURES/8/MEDIUM. URL https://journals.aps.org/prfluids/abstract/10.1103/PhysRevFluids.4.023502.

[14] Marco De Paoli, Sergio Pirozzoli, Francesco Zonta, and Alfredo Soldati. Strong rayleigh–darcy convection regime in three-dimensional porous media. *Journal of Fluid Mechanics*, 943:A51, 7 2022. ISSN 0022-1120. doi: 10.1017/JFM.2022.461. URL https://www.cambridge.org/core/journals/journal-of-fluid-mechanics/article/strong-rayleighdarcy-convection-regime-in-threedimensional-porous-media/78D29B59D5DDA764DDE774F27D4579A0.

[15] A. M. Eckel and R. Pini. Spreading and mixing during solutal convection in uniform porous media with application to geologic co2storage. *Physics of Fluids*, 33, 2021. ISSN 10897666. doi: 10.1063/5.0049287.

[16] Anna-Maria Eckel, Rebecca Liyanage, Takeshi Kurotori, and Ronny Pini. Three-dimensional imaging of dissolution-driven convection in simple porous media using

x-ray ct scanning. *15th International Conference on Greenhouse Gas Control Technologies, GHGT-15*, 2021. doi: 10.2139/SSRN.3811522. URL `https://ssrn.com/abstract=3811522`.

[17] Hamid Emami-Meybodi, Hassan Hassanzadeh, Christopher P Green, and Jonathan Ennis-King. Convective dissolution of co 2 in saline aquifers: Progress in modeling and experiments. *International Journal of Greenhouse Gas Control*, 40:238–266, 2015. doi: 10.1016/j.ijggc.2015.04.003. URL `http://dx.doi.org/10.1016/j.ijggc.2015.04.003`.

[18] Jonathan Ennis-King, Ian Preston, and Lincoln Paterson. Onset of convection in anisotropic porous media subject to a rapid change in boundary conditions. *Physics of Fluids*, 17(8), 2005.

[19] Xiaojing Fu, Luis Cueto-Felgueroso, and Ruben Juanes. Pattern formation and coarsening dynamics in three-dimensional convective mixing in porous media. *Philosophical Transactions of the Royal Society A: Mathematical, Physical and Engineering Sciences*, 371, 12 2013. ISSN 1364503X. doi: 10.1098/rsta.2012.0355.

[20] Ricardo Gasparini. Mesh sensitivity study for cfd simulations. `https://www.simscale.com/knowledge-base/mesh-sensitivity-cfd/`. Accessed: 2024-04-26.

[21] Christopher P. Green and Jonathan Ennis-King. Steady flux regime during convective mixing in three-dimensional heterogeneous porous media. *Fluids*, 3, 9 2018. ISSN 23115521. doi: 10.3390/fluids3030058.

[22] WD Gunter, B Wiwehar, and EH Perkins. Aquifer disposal of co2-rich greenhouse gases: extension of the time scale of experiment for co2-sequestering reactions by geochemical modelling. *Mineralogy and petrology*, 59(1-2):121, 1997.

[23] Francis H Harlow, J Eddie Welch, et al. Numerical calculation of time-dependent viscous incompressible flow of fluid with free surface. *Physics of fluids*, 8(12):2182, 1965.

[24] Duncan R Hewitt, Jerome A Neufeld, and John R Lister. Ultimate regime of high rayleigh number convection in a porous medium. *Physical Review Letters*, 108, 5 2012. doi: 10.1103/PhysRevLett.108.224503.

[25] Duncan R. Hewitt, Jerome A. Neufeld, and John R. Lister. Convective shutdown in a porous medium at high rayleigh number. *Journal of Fluid Mechanics*, 719: 551–586, 2013. ISSN 14697645. doi: 10.1017/jfm.2013.23.

[26] Duncan R Hewitt, Jerome A Neufeld, and John R Lister. High rayleigh number convection in a three-dimensional porous medium. *J. Fluid Mech*, 748:879–895, 2014. doi: 10.1017/jfm.2014.216.

[27] Duncan Robin Hewitt. *High Rayleigh Number Convection in a Porous Medium*. PhD thesis, University of Cambridge, 2013.

[28] Juan J. Hidalgo, Jaime Fe, Luis Cueto-Felgueroso, and Ruben Juanes. Scaling of convective mixing in porous media. *Physical Review Letters*, 109, 12 2012. ISSN 00319007. doi: 10.1103/PhysRevLett.109.264503.

[29] Juan J Hidalgo, Christopher W MacMinn, and Ruben Juanes. Dynamics of convective dissolution from a migrating current of carbon dioxide. *Advances in water resources*, 62:511–519, 2013.

[30] CW Horton and FT Rogers Jr. Convection currents in a porous medium. *Journal of Applied Physics*, 16(6):367–370, 1945.

[31] Charles J Kibert. *Sustainable construction: green building design and delivery*. John Wiley & Sons, 2016.

[32] John Kim and Parviz Moin. Application of a fractional-step method to incompressible navier-stokes equations. *Journal of Computational Physics*, 59:308–323, 1984. URL `https://api.semanticscholar.org/CorpusID:1347299`.

[33] Klaus S Lackner. A guide to co2 sequestration. *New Series*, 300:1677–1678, 2003. doi: 10.1126/science.1083529.

[34] B. Metz, O. Davidson, H. C. De Coninck, M. Loos, and L. A. Meyer. Ipcc, 2005: Ipcc special report on carbon dioxide capture and storage: Technical summary. *Cambridge, United Kingdom and New York, NY, USA*, 442, 2005. URL `https://www.ipcc.ch/site/assets/uploads/2018/03/srccs_wholereport.pdf`.

[35] Itamar Michel-Meyer, Uri Shavit, Avihai Tsinober, and Ravid Rosenzweig. The role of water flow and dispersive fluxes in the dissolution of co2 in deep saline aquifers. *Water Resources Research*, 56, 11 2020. ISSN 19447973. doi: 10.1029/2020WR028184.

[36] Jerome A Neufeld, Marc A Hesse, Amir Riaz, Mark A Hallworth, Hamdi A Tchelepi, and Herbert E Huppert. Convective dissolution of carbon dioxide in saline aquifers. *Geophysical Research Letters*, 37, 11 2010. ISSN 1944-8007. doi: 10.1029/2010GL044728. URL `https://onlinelibrary.wiley.com/doi/abs/10.1029/2010GL044728`.

[37] Paolo Orlandi. *Fluid Flow Phenomena: A Numerical Toolkit*, volume 55. 01 2000. ISBN 978-1-4020-0389-9. doi: 10.1007/978-94-011-4281-6.

[38] Franklin M Orr Jr. Onshore geologic storage of co2. *Science*, 325(5948):1656–1658, 2009.

[39] Jesse Otero, Lubomira A. Dontcheva, Hans Johnston, Rodney Worthing, Alexander Kurganov, Guergana Petrova, and Charles R. Doering. High-rayleigh-number convection in a fluid-saturated porous layer. *Journal of Fluid Mechanics*, 500:263 – 281, 2004. URL `https://api.semanticscholar.org/CorpusID:5775407`.

[40] George S.H. Pau, John B. Bell, Karsten Pruess, Ann S. Almgren, Michael J. Lijewski, and Keni Zhang. High-resolution simulation and characterization of density-driven flow in co2 storage in saline aquifers. *Advances in Water Resources*, 33:443–455, 4 2010. ISSN 03091708. doi: 10.1016/j.advwatres.2010.01.009.

[41] S. Pirozzoli. Revisiting the mixing-length hypothesis in the outer part of turbulent wall layers: mean flow and wall friction. *J. Fluid Mech.*, 745:378–397, 2014.

[42] S. Pirozzoli, M. Bernardini, R. Verzicco, and P. Orlandi. Mixed convection in turbulent channels with unstable stratification. *J. Fluid Mech.*, 821:482–516, 2017.

[43] Sergio Pirozzoli, Marco De Paoli, Francesco Zonta, and Alfredo Soldati. Towards the ultimate regime in rayleigh-darcy convection. *Journal of Fluid Mechanics*, 911, 2021. ISSN 14697645. doi: 10.1017/jfm.2020.1178.

[44] Stephen B. Pope. *Turbulent Flows*. Cambridge University Press, 2000.

[45] Julius Reiss. A family of energy stable, skew-symmetric finite difference schemes on collocated grids: a simple way to avoid odd–even decoupling. *Journal of Scientific Computing*, 65:821–838, 2015.

[46] A. Riaz, M. Hesse, H. A. Tchelepi, and F. M. Orr. Onset of convection in a gravitationally unstable diffusive boundary layer in porous media. *Journal of Fluid Mechanics*, 548:87–111, 2 2006. ISSN 14697645. doi: 10.1017/S0022112005007494.

[47] Patrick J Roache. Perspective: a method for uniform reporting of grid refinement studies. 1994.

[48] Anja C. Slim. Solutal-convection regimes in a two-dimensional porous medium. *Journal of Fluid Mechanics*, 741:461–491, 2014. ISSN 14697645. doi: 10.1017/jfm.2013.673.

[49] Anja C Slim, Mahesh M Bandi, Joel C Miller, and Lakshminarayanan Mahadevan. Dissolution-driven convection in a hele–shaw cell. *Physics of Fluids*, 25(2), 2013.

[50] M. L. Szulczewski, M. A. Hesse, and R. Juanes. Carbon dioxide dissolution in structural and stratigraphic traps. *Journal of Fluid Mechanics*, 736:287–315, 12 2013. ISSN 14697645. doi: 10.1017/jfm.2013.511.

[51] Bert Van Der Meer. Carbon dioxide storage in natural gas reservoir. *Oil & gas science and technology*, 60(3):527–536, 2005.

[52] Baole Wen, Daria Akhbari, Li Zhang, and Marc A. Hesse. Convective carbon dioxide dissolution in a closed porous medium at low pressure. *Journal of Fluid Mechanics*, 854:56–87, 11 . ISSN 0022-1120. doi: 10.1017/JFM.2018.622. URL `https://www.cambridge.org/core/journals/journal-of-fluid-mechanics/article/abs/convective-carbon-dioxide-dissolution-in-a-closed-porous-medium-at-low-pressure/FBA6A1738D6BE9D95B42209DD36489F0`.

[53] Francesco Zonta and Alfredo Soldati. Stably stratified wall-bounded turbulence. 70(4):040801. ISSN 0003-6900. doi: 10.1115/1.4040838. URL `https://doi.org/10.1115/1.4040838`.